PUBLICATIONS OF THE ASTRONOMICAL SOCIETY OF THE PACIFIC, **113**:10–28, 2001 January

A New Complete Sample of Submillijansky Radio Sources: An Optical and Near-Infrared Study

FRANK J. MASCI,[1,2] J. J. CONDON,[3] T. A. BARLOW,[1] C. J. LONSDALE,[1] C. XU,[1]
D. L. SHUPE,[1] O. PEVUNOVA,[1,4] F. FANG,[1] AND R. CUTRI[1]
Received 2000 August 2; accepted 2000 October 5

ABSTRACT. The Very Large Array has been used in C configuration to map an area $\simeq$0.3 deg^2 at 1.4 GHz with 5 σ sensitivities of 0.305, 0.325, 0.380, and 0.450 mJy beam^{-1} over four equal subareas. Radio properties are presented for 62 detected sources. Deep optical imaging to Gunn $r \simeq 25$ mag using the Hale 5 m telescope covering $\simeq$0.21 deg^2 is reported for a subset of 43 sources. This optical follow-up is much deeper than that of existing larger area radio surveys of similar radio sensitivity. Archival *J*-, *H*-, and *K*-band photometry from the Two-Micron All Sky Survey is also presented. Using a robust likelihood ratio technique, we optically identified 26 radio sources with probabilities $\gtrsim$80%, nine with uncertain/ambiguous detections, and eight with empty fields. Comparisons with a stellar synthesis model that includes radio emission and dust reddening suggest that the near-infrared–optical emission in a small, bright subsample is reddened by "optically thin" dust with absorption $A_V \simeq 2$–2.5 mag, regardless of morphological type. This is consistent with other, more direct determinations of absorption. The radio–optical(–near-infrared) flux ratios of early-type galaxies require significant contamination in the radio by an active galactic nucleus, consistent with the current paradigm. Using our simple modeling approach, we also discuss a potential diagnostic for selecting ultraluminous infrared galaxies to $z \simeq 1.6$ from microjansky radio surveys.

1. INTRODUCTION

The advent of deep radio surveys reaching flux densities well below 1 mJy (Mitchell & Condon 1985; Windhorst et al. 1985, 1993; Oort 1987; Hopkins et al. 1998; Richards 2000) revealed a new population of faint sources more numerous than the active galactic nucleus (AGN) powered radio galaxies dominating the strong-source population. This corresponds to a steepening of the differential source counts over nonevolving predictions at levels $\lesssim$4 mJy. The faint counts suggest that significant evolution has occurred over the redshift range spanned by the observed population. Photometric and spectroscopic studies (Thuan et al. 1984; Windhorst et al. 1985; Thuan & Condon 1987; Benn et al. 1993) suggest that the faint excess at 1.4 GHz is composed predominantly of star-forming galaxies similar to the nearby starburst population dominating the *Infrared Astronomical Satellite* (*IRAS*) 60 μm counts (Benn et al. 1993). Indeed, this is supported by the strong correlation between radio (1.4 GHz) and far-infrared (60 μm) flux densities of disk galaxies (Helou, Soifer, & Rowan-Robinson 1985), implying a significant proportion of starburst galaxies at faint radio flux densities.

The overall observed source-count distribution from faint (microjansky [μJy]) to bright ($S_{1.4} \gtrsim 10$ mJy) flux densities cannot be explained by starbursts alone. Evolutionary models of radio source counts need to invoke two separate populations (e.g., Danese et al. 1987; Rowan-Robinson et al. 1993; Hopkins et al. 1998). Condon (1989) describes these populations as starbursts and monsters, each powered by different mechanisms: "starbursts" deriving their radio emission from supernova remnants and H II regions, and "monsters" from compact nuclear related activity (e.g., AGNs). The proportion of AGNs is much greater at higher flux densities $S_{1.4} \gtrsim 10$ mJy (Kron, Koo, & Windhorst 1985; Gruppioni, Mignoli, & Zamorani 1999), where a majority are associated with classical radio galaxies exhibiting extended (FR I and FR II type) morphologies (Fanaroff & Riley 1974). The optical counterparts to sources at bright radio flux densities $S_{1.4} \gtrsim 1$ mJy are composed mostly of elliptical galaxies, while at submillijansky (sub-mJy) to μJy levels the optical counterparts are identified as blue galaxies exhibiting peculiar (compact, interacting, and irregular) morphologies (Kron et al. 1985; Gruppioni et al. 1999). Studies of faint radio sources, namely, their stellar population, how they evolve with redshift, and how they relate to local normal galaxies are progressing rapidly; however, much remains to be learned from the faintest (μJy) radio populations at redshifts $1 \lesssim z \lesssim 2$.

Radio surveys are insensitive to the effects of absorption by

[1] Infrared Processing and Analysis Center, M/S 100-22, California Institute of Technology, Jet Propulsion Laboratory, Pasadena, CA 91125.
[2] fmasci@ipac.caltech.edu.au.
[3] National Radio Astronomy Observatory, 520 Edgemont Road, Charlottesville, VA 22903.
[4] Present address: Interferometry Science Group, M/S 171-122C, Jet Propulsion Laboratory, Pasadena, CA 91109-8099.

dust, which is known to bias surveys severely at optical-UV wavelengths. This is particularly important for derivations of the cosmic history of star formation and its relation to hierarchical models of galaxy formation. Optical-UV studies have shown that there is an increase in both the space density of star-forming, morphologically disturbed galaxies (e.g., Richards et al. 1999) and the global star formation rate with redshift to $z \gtrsim 1$ (e.g., Madau et al. 1996). Similar evidence is emerging from studies of submillimeter sources (Blain et al. 1999) and amongst the faint radio population at $1 \lesssim z \lesssim 2$—the redshift range probed by the deepest surveys (e.g., Cram 1998; Haarsma et al. 1999).

There has been much speculation as to whether global star formation rates (SFRs) derived from radio observations exceed those determined from optical-UV studies. Cram et al. (1998) note that systematic discrepancies may exist between the various star formation indicators, which are not well understood (see also Schaerer 1999). It is encouraging to see, however, that Haarsma et al. (2000) find global SFRs derived from 1.4 GHz observations of the Hubble Deep Field to exceed optically determined values by a factor of a few out to $z \sim 1$. Indeed, an analysis of Balmer decrements and optical–near-infrared colors in star-forming galaxies by Georgakakis et al. (1999) from the Phoenix Deep Survey (Hopkins et al. 1998) finds evidence for visual extinctions from 1 to a few mag. Currently, about 20% of existing μJy radio samples remain unidentified to $I = 25$ mag in Hubble Deep Field images (e.g., Richards et al. 1999). A majority of these could represent a significant population of dust-enshrouded starbursts and/or AGNs at high redshift. These results are in support of efforts to further understand the dust properties of star-forming galaxies.

The primary aim of this paper is to introduce a new complete sample of radio sources selected at 1.4 GHz, uniformly selected over the flux range $S \gtrsim 0.3$ mJy (5 σ) from an area covering $\simeq 0.3$ deg^2. Although much larger area surveys to deeper radio sensitivities have been carried out (e.g., Hopkins et al. 1998), the present study reports the results of more sensitive optical observations. Archival near-IR data for a subset of the sample are also presented. The near-IR data are from the ongoing 2MASS project and represent a unique aspect of this study in the identification of radio-selected starbursts. Although we currently lack valuable spectroscopic information, we combine radio–near-IR–optical flux ratios, radio maps, and optical images to explore the properties of the entire sample. Our deep optical identifications provide the opportunity to asses the importance of dust in star-forming systems via the observed radio-optical and near-IR–optical colors. Simple stellar synthesis models that include radio emission and reddening are used to constrain possible amounts of absorption.

This paper is organized as follows. In § 2, we discuss the radio observations and data reduction, present the radio catalog, and compare our results with data available from (shallower) all-sky radio surveys. The optical photometric observations, their reduction, and astrometric calibrations are discussed in § 3. Our method for radio-optical identification, the archival near-IR data, radio-optical image overlays, and our optical–near-IR catalog are presented in § 4. A study of the radio, near-IR, and optical colors and constraints on synthesis models incorporating dust is presented in § 5. An application of our color-color analysis to select high-redshift ultraluminous infrared galaxies from deep radio surveys is discussed in § 6. All results and future prospects are summarized in § 7.

2. RADIO OBSERVATIONS

2.1. Strategy

Observations were made with the VLA C configuration at 1.4 GHz on 1998 December 19. This configuration yields a good compromise for resolution and surface brightness sensitivity. The 5 σ confusion limit for this configuration is only 50 μJy beam^{-1} at 1.4 GHz (Mitchell & Condon 1985) since the synthesized beam size (full width at half-power [FWHP]) is $\sim$15″. The resulting radio positions have rms errors $\sim$1″, except for extended sources with multiple components, sufficient for making optical identifications. At 1.4 GHz the FWHP of the VLA primary beam is 31′ and approximately corresponds to the diameter of our final imaged field. This relatively large coverage avoids field-to-field variations in source counts induced by high-redshift clustering. Although surveys at higher frequencies (e.g., 8 GHz) can reach lower flux densities than at 1.4 GHz, most radio sources have spectral indices $\alpha \sim 1$ ($S \propto \nu^{-\alpha}$), so the population being sampled is similar.

To provide uniform sensitivity over the full area of our field, we observed seven positions arranged in a filled hexagonal pattern with a separation of 26′ between pointing centers. The resulting rms map noise is thus nearly constant (cf. Condon et al. 1998). Our field was centered on R.A.(J2000) = $00^h13^m12\overset{s}{.}0$, decl.(J2000) = +25°54′44″. This field was chosen for its relatively low foreground galactic-cirrus emission which is likely to affect optical–near-IR identifications and also for the absence of bright radio galaxies. The integration time on each pointing was $\sim$1 hour. This allowed us to reach an rms noise of $\sim$60 μJy in regions free from bright contaminating sources (see § 2.3 for more details).

Our observations were made in spectral line mode with four intermediate frequencies (IFs), each divided into seven spectral channels of width 3.125 MHz. The advantage of this mode is to minimize bandwidth smearing (i.e., chromatic aberration) which reduces the point-source sensitivity away from the pointing center and causes appreciable image distortion. Additionally, the spectral line mode is less prone to narrowband interference noise spikes. With continuum mode, however, we would have had a little over twice the bandwidth and a factor $\approx\sqrt{2}$ lower noise.

2.2. Data Reduction

The data were analyzed with the NRAO AIPS reduction package. We observed 3C 48 to calibrate the visibility amplitudes,

TABLE 1
THE REGIONS USED FOR THE SOURCE EXTRACTIONS

Region	R.A. (J2000)[a]	Decl. (J2000)[a]	σ_{rms} (mJy)	5 σ Limit (mJy)	No. of Sources[b]
1	00 13 48.43	+25 48 07.7	0.061	0.305	15
2	00 12 34.09	+25 47 11.7	0.065	0.325	15
3	00 12 33.11	+26 03 27.7	0.090	0.450	20
4	00 13 48.21	+26 02 47.7	0.076	0.380	14[c]

NOTE.—Units of right ascension are hours, minutes, and seconds, and units of declination are degrees, arcminutes, and arcseconds.

[a] Defines the center of each region with size ≈16.5 × 16.5 arcmin^2.

[b] Total number of sources with flux density ≥5 σ_{rms}.

[c] Includes the separate components of two double-component sources.

using $S = 16.5$ and $S = 15.9$ Jy at 1.365 and 1.435 GHz, respectively. The calibration was applied using the *split* task. The calibrated data from each pointing were edited and imaged separately, CLEANed, and restored with 15″ FWHP Gaussian beams. The seven separate images were weighted and combined as described in Condon et al. (1998) to produce a final 33′ × 33′ map with nearly uniform sensitivity and corrected for primary-beam attenuation.

2.3. Noise and Source Extractions

The resulting rms noise of our final map after correcting for primary-beam attenuation is not uniform over the entire field but increases by up to 30% near a strong (≳400 mJy) source near the edge of our field. Despite this variation in sensitivity, we were able to divide our 33 × 33 arcmin^2 field into four equal (≈16.5 × 16.5 arcmin^2) regions within which the rms noise varies by no more than a few percent. These constant-noise regions simplify the application of an automated source-finding algorithm over a single continuous region (see below). The lowest and highest rms noise amongst these regions was ≃60.9 and ≃90.3 μJy beam^{-1}, respectively. See Table 1 for the region definitions. The rms noise of each region was estimated from the Gaussian core of the amplitude distribution of the pixel values as produced by the AIPS task *imean*. In Figure 1, we show the distribution in pixel values of our entire 33′ field. The rms deviation in peak flux density derived from a fit to this histogram is ≃69 μJy beam^{-1}. Figure 2 shows a contour map of our entire radio field.

Each constant-noise region in Table 1 was used for the source extractions. Within each region, we searched for radio sources down to a peak flux density ≥5 times the rms value of the region. The sources were extracted by the AIPS task *sad*, which uses Gaussian fits to estimate the fluxes, positions, and angular sizes of the selected sources. However, for faint sources, unconstrained Gaussian fits may be unreliable (see Condon 1997). For this reason, we adopted the following method for the source extraction: first, we ran the task *sad* with a 3 σ_{rms} detection threshold to obtain an initial list of candidates; we then derived the peak flux densities of the faint sources (with 3 $\sigma < S_{peak} < 7$ σ) using the *maxfit* task. This task uses a second-order

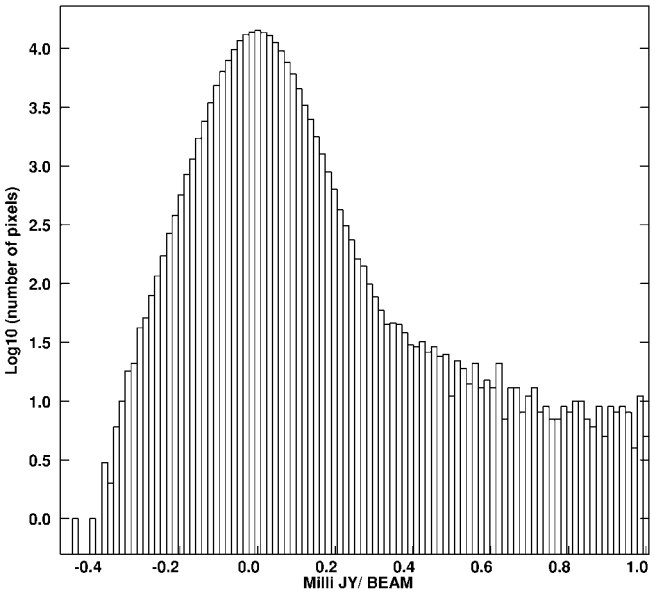

FIG. 1.—Logarithmic histogram of pixel flux densities in our complete radio map.

interpolation algorithm and is known to be more accurate. Only sources with a *maxfit* peak flux density ≥5 σ_{rms} were retained. For these faint sources, the total flux density was estimated using the task *imean*, which integrates the (median background subtracted) pixel values in a specific rectangle. The rectangle

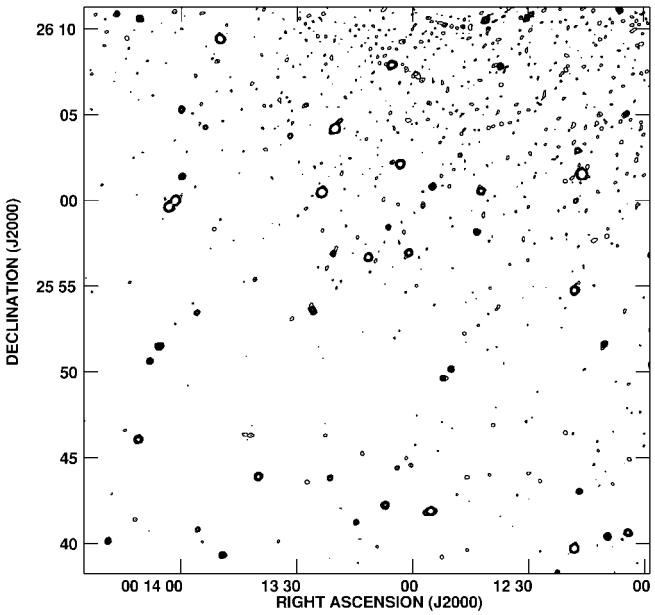

FIG. 2.—Contour plot of our radio map covering an area 33 × 33 arcmin^2 = 495 × 495 pixels. Contour levels are 0.2, 0.4, 0.6, 0.8, 1.0, 1.2, 1.4, 1.6 mJy beam^{-1}. Note the increase in rms noise from the bright off-field source in the top right corner.

was chosen to encompass as much of the source as possible. For all other parameters (sizes, positions, and position angles) we retained the values obtained from the initial Gaussian fits. Only two sources had irregular morphologies showing multiple components. For these, the total (background subtracted) flux was determined using the task *tvstat*, which allows an integration over a specific irregular area defined to encompass as much of the source as possible.

The numbers of sources detected in each constant-noise region are summarized in Table 1. A total of 62 sources were detected with flux densities $\geq 5\ \sigma_{\rm rms}$ over an area of 0.303 deg^2. Within Poisson uncertainties, this number is consistent with source counts from surveys by Ciliegi et al. (1999) and Hopkins et al. (1998). To our limiting (mean) sensitivity of 0.35 mJy and within 0.303 deg^2, they report a source count of typically 70 ± 8. This confirms the reliability of our radio source detections and flux density estimates.

Table 2 shows the full radio catalog which reports (in column order) (1) the source name; (2) right ascension (R.A.[J2000]) and (3) declination (decl.[J2000]); errors in (4) R.A. and (5) decl.; (6) the peak flux density S_P; (7) error in S_P; (8) the total flux density S_T; (9) error in S_T; the FWHM of the major and minor axes (10) θ_M and (11) θ_m (determined from Gaussian fits); (12) the position angle (P.A.) of the major axis (in degrees); and the rms errors associated with (13) θ_M, (14) θ_m, and (15) P.A., respectively. The different components of multiple sources are labeled "C1" and "C2." In Figure 3, we show the distribution of peak flux densities and the total/peak flux ratio as a function of peak flux for all sources. Sources with ratios $S_T/S_P < 1$ in Figure 3*b* are primarily the result of uncertainties on measured fluxes as estimated from the two-dimensional Gaussian fits. Uncertainties in peak fluxes are typically $\lesssim$10%, while total flux estimates are more uncertain due to a sensitive dependence on the Gaussian fitting procedure. Errors in total fluxes are typically $\lesssim$30%. Contour maps of radio sources with available optical data are shown inFigure 8.

2.4. Comparison with the NVSS Catalog

The 33×33 arcmin^2 region that we observed with the VLA was also covered by the NRAO VLA Sky Survey (NVSS; Condon et al. 1998). The NVSS covers the sky north of $\delta = -40°$ at 1.4 GHz with 45″ resolution and limiting flux density $\simeq$2.25 mJy (5 σ). To this limit, 17 of our sources were found to be in common with the NVSS public catalog. However, one source in our catalog is a double-component source and is unresolved by the NVSS. A comparison of flux densities derived in this study with those from that catalog is shown in Figure 4. It is evident that our derived flux densities are on average slightly lower than those from the NVSS. This was also reported in a larger comparison study by Ciliegi et al. (1999) using a similar observational setup and can be explained by the difference in resolutions used in the two surveys: 15″ here versus 45″ there. High-resolution surveys tend to miss flux from low surface brightness emission. Although the effect is only marginal for bright sources, it may become important for attempts to detect faint, low surface brightness objects at high redshift.

3. OPTICAL PHOTOMETRIC OBSERVATIONS

3.1. Observations and Data Reduction

Optical CCD photometry of our radio field was carried out on the 5 m Hale telescope at Palomar Observatory[5] during the nights of 1997 August 27–29. These fields were initially selected for subsequent deep mid-IR imaging with the *Wide Field Infrared Explorer* mission (*WIRE*), but the mission failed to perform to expectations. The Carnegie Observatories Spectroscopic Multislit and Imaging Camera (COSMIC; Kells et al. 1998) mounted at the f/3.5 prime focus with a Tek 2K CCD was used to image nine 9.7×9.7 arcmin^2 fields in the Gunn r (6550 Å) filter. Each optical field was composed of three optical pointings offset by 2′, each with integrations of 600 s, giving a total 1800 s per field. This resulted in a limiting magnitude of $r \simeq 25$ mag (5 σ). The seeing was typically 1″–1.″4 (FWHM). The optical fields do not cover our entire 33×33 arcmin^2 radio field. The nine slightly overlapping optical fields correspond to an areal coverage 27.5×27.5 arcmin^2, or about 70% of the radio map.

The CCD data were reduced with standard tasks in the IRAF package. Frames were first bias-subtracted, then flat-fielded using dome flats. Bad pixels and columns were removed by interpolating between adjacent pixels. Finally, the individual dithered frames were median combined to remove cosmic-ray hits. Calibration was performed using standard stars from Thuan & Gunn (1976). These were used to correct for atmospheric extinction from varying air mass and provide the instrumental zero point. Photometric uncertainties, estimated using these standards, are no more than $\approx$0.05 mag.

Sources in the reduced optical frames were extracted using the DAOPHOT package in IRAF (Stetson 1987). This package has the benefit of performing photometry in crowded fields, which is the case in most regions of our optical fields. It performed the following steps: first, sources were extracted above a given threshold, given as a multiple of the total CCD noise (sky and read noise, $\sigma_{\rm tot}$). We adopted threshold values of 4.5–5 $\sigma_{\rm tot}$, just high enough to avoid large numbers of spurious detections. Second, simple aperture photometry was performed on these identified sources. This required a specification of the aperture radius which is likely to contain most of the light of our target source and of the width of a surrounding annulus to estimate and subtract the sky background. We adopted a radius of 6″ and annulus width of 4″. Next, a point-spread function (PSF) was determined in each of our nine fields. This involved an iterative technique to remove contamination from neighboring sources in crowded fields near our PSF can-

[5] Operated by California Institute of Technology, Pasadena, CA 91125.

TABLE 2
CATALOG OF RADIO SOURCE DATA

Name (1)	R.A. (J2000) (2)	Decl. (J2000) (3)	$\sigma_{\rm R.A.}$ (arcsec) (4)	$\sigma_{\rm Decl.}$ (arcsec) (5)	S_P (mJy) (6)	σ_{S_P} (mJy) (7)	S_T (mJy) (8)	σ_{S_T} (mJy) (9)	θ_M (arcsec) (10)	θ_m (arcsec) (11)	P.A. (deg) (12)	σ_{θ_M} (arcsec) (13)	σ_{θ_m} (arcsec) (14)	$\sigma_{\rm P.A.}$ (deg) (15)
RAD J001158+2550	00 11 58.058	+25 50 24.41	0.37	0.43	1.468	0.095	1.410	0.088	15.944	13.579	169	1.027	0.875	16
RAD J001158+2556	00 11 58.078	+25 56 48.20	0.24	0.26	2.176	0.095	2.820	0.075	14.482	12.969	24	0.630	0.564	16
RAD J001203+2544	00 12 03.977	+25 44 54.18	1.35	1.06	0.424	0.084	0.284	0.116	15.249	9.908	63	3.402	2.210	20
RAD J001204+2540	00 12 04.313	+25 40 37.21	0.22	0.21	2.653	0.092	2.930	0.118	15.797	13.559	51	0.563	0.484	9
RAD J001204+2605	00 12 04.572	+26 05 01.42	0.66	0.61	0.973	0.084	0.962	0.036	18.466	12.055	129	1.795	1.172	9
RAD J001206+2611	00 12 06.178	+26 11 05.20	0.49	0.59	1.096	0.095	1.050	0.046	16.439	13.115	19	1.419	1.132	15
RAD J001209+2540	00 12 09.614	+25 40 24.41	0.30	0.31	1.880	0.093	2.780	0.099	14.993	14.237	29	0.755	0.717	39
RAD J001210+2551	00 12 10.381	+25 51 36.54	0.40	0.43	1.402	0.094	1.300	0.110	16.091	12.989	147	1.086	0.876	13
RAD J001216+2601	00 12 16.041	+26 01 31.64	0.03	0.03	17.676	0.064	18.42	0.108	17.051	15.245	10	0.091	0.081	2
RAD J001216+2543	00 12 16.854	+25 43 02.09	0.60	0.57	0.955	0.084	0.836	0.140	14.521	13.550	100	1.437	1.341	58
RAD J001217+2602	00 12 17.177	+26 02 53.96	0.73	0.61	0.878	0.044	0.844	0.159	16.079	13.462	99	1.732	1.450	24
RAD J001218+2554	00 12 18.056	+25 54 44.99	0.13	0.13	4.580	0.095	4.700	0.173	15.301	15.081	47	0.316	0.311	18
RAD J001218+2539	00 12 18.193	+25 39 42.82	0.07	0.07	8.443	0.095	8.380	0.167	14.927	14.783	16	0.167	0.166	17
RAD J001227+2543	00 12 27.184	+25 43 39.10	3.09	3.67	0.240	0.090	0.408	0.207	26.143	14.623	144	9.884	5.529	25
RAD J001230+2610	00 12 30.123	+26 10 40.53	1.38	1.35	0.734	0.098	1.141	0.201	33.900	13.072	134	4.253	1.640	5
RAD J001237+2607	00 12 37.254	+26 07 48.87	0.54	0.53	1.157	0.089	1.230	0.147	16.823	14.221	49	1.375	1.163	20
RAD J001240+2609	00 12 40.394	+26 09 57.71	1.18	1.57	0.447	0.094	0.419	0.157	18.876	11.192	153	3.994	2.368	16
RAD J001241+2610	00 12 41.007	+26 10 31.16	0.31	0.28	2.006	0.071	1.970	0.116	16.611	13.268	121	0.783	0.626	8
RAD J001242+2600	00 12 42.209	+26 00 33.55	0.18	0.18	3.229	0.095	4.160	0.086	15.278	14.392	62	0.448	0.422	20
RAD J001243+2558	00 12 43.323	+25 58 10.05	0.51	0.50	1.158	0.095	1.130	0.136	15.394	14.207	52	1.257	1.160	41
RAD J001246+2543	00 12 46.030	+25 43 51.08	2.24	1.63	0.344	0.093	0.410	0.123	19.944	13.441	107	5.430	3.659	17
RAD J001247+2602	00 12 47.680	+26 02 38.49	0.86	0.90	0.559	0.094	0.377	0.127	12.744	11.914	21	2.155	2.014	12
RAD J001250+2550	00 12 50.036	+25 50 10.68	0.45	0.46	1.224	0.095	1.050	0.151	14.153	13.629	26	1.094	1.054	83
RAD J001252+2549	00 12 52.006	+25 49 38.49	1.21	0.88	0.655	0.033	0.855	0.130	20.303	14.466	82	2.881	2.053	17
RAD J001254+2600	00 12 54.835	+26 00 48.52	0.34	0.34	1.656	0.095	1.490	0.125	14.504	13.978	130	0.829	0.799	63
RAD J001255+2541	00 12 55.365	+25 41 53.48	0.14	0.12	4.717	0.094	5.470	0.182	17.566	14.852	96	0.351	0.296	5
RAD J001257+2559	00 12 57.288	+25 59 43.59	0.84	1.33	0.544	0.093	0.553	0.155	18.083	11.514	179	3.141	2.000	15
RAD J001259+2607	00 12 59.107	+26 07 18.91	1.86	1.44	0.497	0.089	0.501	0.218	24.476	18.828	84	4.406	3.390	27
RAD J001300+2556	00 13 00.983	+25 56 57.10	0.18	0.18	3.230	0.095	4.070	0.096	15.100	14.147	129	0.442	0.414	18
RAD J001303+2602	00 13 03.185	+26 02 07.41	0.11	0.11	5.136	0.095	5.270	0.097	15.289	15.108	112	0.282	0.278	23

RAD J001304+2544	00 13 04.017	+25 44 25.38	0.89	0.96	0.545	0.094	0.977	0.129	13.924	11.175	146	2.416	1.939	32
RAD J001305+2607	00 13 05.397	+26 07 54.15	0.18	0.16	3.906	0.093	4.990	0.119	19.377	14.842	115	0.462	0.354	4
RAD J001307+2542	00 13 07.094	+25 42 14.25	0.25	0.25	2.384	0.095	3.380	0.091	15.068	14.900	7	0.598	0.591	13
RAD J001311+2556	00 13 11.484	+25 56 41.98	0.12	0.12	4.782	0.095	4.900	0.076	14.915	14.203	150	0.295	0.281	16
RAD J001313+2545	00 13 13.019	+25 45 15.15	1.57	1.75	0.358	0.094	0.529	0.155	17.375	11.916	36	4.588	3.147	28
RAD J001314+2541	00 13 14.646	+25 41 14.85	0.74	0.80	0.723	0.074	0.824	0.121	14.606	13.296	162	1.909	1.738	16
RAD J001318+2604C1	00 13 18.834	+26 04 38.76	1.28	1.09	0.578	0.093	0.597	0.156	22.405	9.339	128	3.666	1.528	7
RAD J001320+2604C2	00 13 20.122	+26 04 11.43	0.05	0.05	12.512	0.092	13.44	0.081	17.148	14.930	130	0.129	0.113	2
RAD J001320+2556	00 13 20.552	+25 56 55.59	0.58	0.71	0.911	0.094	0.993	0.154	17.319	11.884	151	1.797	1.233	11
RAD J001321+2543	00 13 21.405	+25 43 49.37	0.69	0.70	0.800	0.096	0.888	0.148	14.764	13.115	140	1.745	1.551	10
RAD J001323+2600	00 13 23.522	+26 00 29.25	0.03	0.03	15.877	0.095	16.24	0.097	15.258	15.080	130	0.091	0.090	21
RAD J001325+2553	00 13 25.931	+25 53 37.18	0.56	0.70	1.170	0.092	1.700	0.210	22.747	14.340	30	1.791	1.129	7
RAD J001327+2543	00 13 27.289	+25 43 35.07	1.29	1.22	0.424	0.094	0.332	0.119	13.870	12.706	64	3.091	2.832	13
RAD J001339+2543	00 13 39.899	+25 43 54.55	0.18	0.18	3.140	0.065	4.010	0.161	14.983	14.384	141	0.451	0.433	30
RAD J001342+2546	00 13 42.203	+25 46 18.76	2.95	1.55	0.361	0.030	0.654	0.237	27.823	14.628	92	6.953	3.656	15
RAD J001349+2539	00 13 49.176	+25 39 20.08	0.42	0.35	1.519	0.035	1.450	0.162	16.018	13.413	88	0.998	0.835	14
RAD J001349+2609	00 13 49.935	+26 09 25.19	0.10	0.10	6.301	0.094	7.330	0.088	17.944	14.591	46	0.268	0.218	3
RAD J001350+2608	00 13 50.742	+26 08 06.93	1.31	1.04	0.460	0.094	0.364	0.110	15.341	11.627	107	3.153	2.390	30
RAD J001355+2540	00 13 55.638	+25 40 48.82	1.12	1.15	0.538	0.094	0.547	0.165	16.771	13.643	138	2.945	2.396	34
RAD J001355+2553	00 13 55.874	+25 53 27.52	0.73	0.72	0.760	0.097	1.432	0.135	15.362	12.182	133	1.912	1.516	22
RAD J001359+2601	00 13 59.764	+26 01 23.68	0.41	0.39	1.413	0.095	1.360	0.045	15.092	13.286	124	1.011	0.890	21
RAD J001359+2605	00 13 59.945	+26 05 17.72	0.49	0.63	1.080	0.095	1.090	0.087	17.033	13.351	175	1.492	1.169	14
RAD J001401+2559C1	00 14 01.544	+25 59 59.45	0.06	0.07	9.410	0.094	9.860	0.132	17.264	15.048	150	0.173	0.151	3
RAD J001401+2610	00 14 01.825	+26 10 59.96	1.14	1.04	0.465	0.084	0.329	0.120	13.499	11.792	114	2.742	2.395	31
RAD J001403+2559C2	00 14 03.162	+25 59 37.11	0.08	0.08	8.005	0.088	9.080	0.028	16.501	15.463	140	0.195	0.182	7
RAD J001405+2551	00 14 05.675	+25 51 29.74	0.37	0.30	1.884	0.095	2.100	0.081	17.524	14.319	90	0.879	0.719	10
RAD J001408+2550	00 14 08.057	+25 50 37.67	0.50	0.47	1.172	0.035	1.650	0.072	14.896	13.522	113	1.202	1.091	24
RAD J001410+2610	00 14 10.909	+26 10 35.97	0.32	0.30	1.828	0.095	1.870	0.094	15.161	13.586	60	0.785	0.703	19
RAD J001411+2546	00 14 11.017	+25 46 03.46	0.23	0.20	2.919	0.095	3.190	0.110	16.703	14.714	93	0.541	0.477	10
RAD J001411+2541	00 14 11.856	+25 41 24.11	1.19	1.40	0.417	0.088	0.331	0.140	14.811	12.073	19	3.356	2.736	45
RAD J001416+2610	00 14 16.812	+26 10 51.50	0.86	0.94	0.681	0.093	0.696	0.126	16.754	13.742	149	2.327	1.909	28
RAD J001418+2540	00 14 18.769	+25 40 08.27	0.49	0.54	1.107	0.095	1.200	0.110	15.381	13.182	150	1.314	1.126	12

NOTE.—Units of right ascension are hours, minutes, and seconds, and units of declination are degrees, arcminutes, and arcseconds.

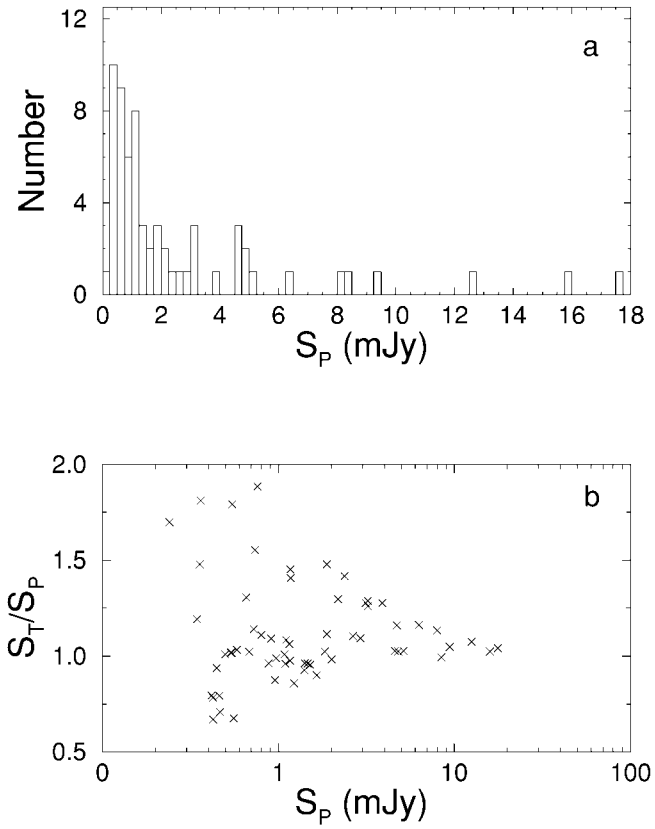

FIG. 3.—(*a*) Distribution of peak flux density and (*b*) total/peak flux ratio as a function of peak flux.

didates. Simultaneous PSF fitting on all sources was then performed to identify sources which were previously hidden in crowded regions. Finally, the magnitudes determined from PSF fits were aperture corrected to a common aperture size as used on our standard stars. Aperture corrections were typically 0.22 mag. A final visual inspection removed any spurious detections. A total of ≈300–390 sources were extracted from each 9.7×9.7 arcmin^2 field to a limit of $r \simeq 25$ mag. Previous optical surveys find typically 380–520 sources within this area to this limit, and the variation is primarily due to clustering. Such fluctuations are found to be significant on such relatively small scales (e.g., Metcalfe et al. 1991).

3.2. Astrometry

The astrometry on the optical images was based on 10–12 APM catalog stars in each field (Maddox et al. 1990). The *ccmap* and *cctran* tasks in the IRAF *immcoords* package were used to compute plate solutions relating pixel positions to astrometric coordinates. Astrometric coordinates for all sources on the frames were then determined. By comparing the positions of several sources common to the APM catalog and our fields, we found that our rms position uncertainties are typically $\lesssim 0\farcs9$.

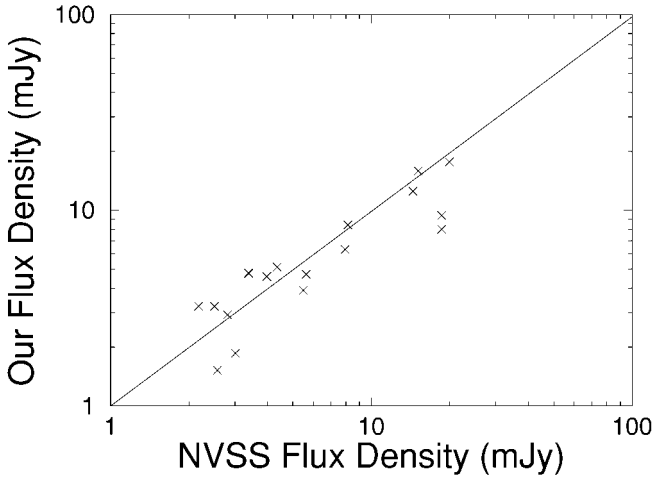

FIG. 4.—The peak flux density obtained with our survey vs. that reported for the same sources in the NVSS public database.

4. OPTICAL–NEAR-INFRARED IDENTIFICATION OF RADIO SOURCES

4.1. Method for Optical Identification

We assigned optical identifications and estimate their reliability using a robust likelihood ratio (LR) analysis. This general method has frequently been used to assess identification probabilities for radio and infrared sources (e.g., de Ruiter, Willis, & Arp 1977; Prestage & Peacock 1983; Sutherland & Saunders 1992; Lonsdale et al. 1998). The method, which computes the probability that a suggested identification is the "true" optical counterpart, is outlined as follows.

For each optical candidate i in the search area of some radio source j, we calculated the value of the dimensionless difference in radio and optical positions:

$$r_{ij} = \left[\frac{(\alpha_i - \alpha_j)^2}{\sigma_{\alpha_i}^2 + \sigma_{\alpha_j}^2} + \frac{(\delta_i - \delta_j)^2}{\sigma_{\delta_i}^2 + \sigma_{\delta_j}^2}\right]^{1/2}, \quad (1)$$

where the α and δ terms represent right ascensions and declinations, respectively, and the σ terms standard deviations. We chose a moderately large search radius of $10''$ to allow for the maximal position uncertainties: $\sigma_{\rm opt} \approx 1\farcs4$ and $\sigma_{\rm rad} \approx 1\farcs5$ [assuming 5 $\sigma_{\rm eff}$, where $\sigma_{\rm eff} = (\sigma_{\rm opt}^2 + \sigma_{\rm rad}^2)^{1/2}$]. Such a radius is also small enough to avoid large numbers of chance associations.

Given r_{ij}, we must now distinguish between two mutually exclusive possibilities: (1) the candidate is a confusing background object that happens to lie at distance r_{ij} from the radio source, or (2) the candidate is the "true" identification that appears at distance r_{ij} owing solely to radio and optical position uncertainties. We assume that the radio and optical positions would coincide if these uncertainties were zero. However, this

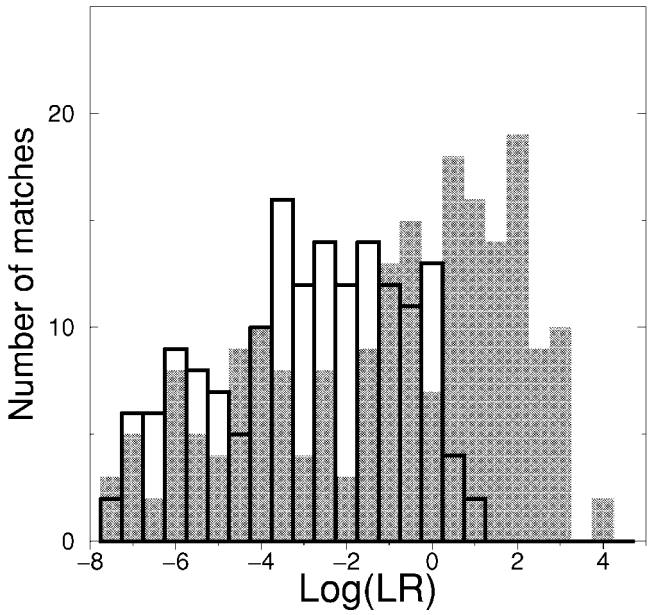

FIG. 5.—Distribution of LR for radio-optical matches at "true" radio positions (*shaded histogram*), and at "random" radio positions (*thick-lined histogram*).

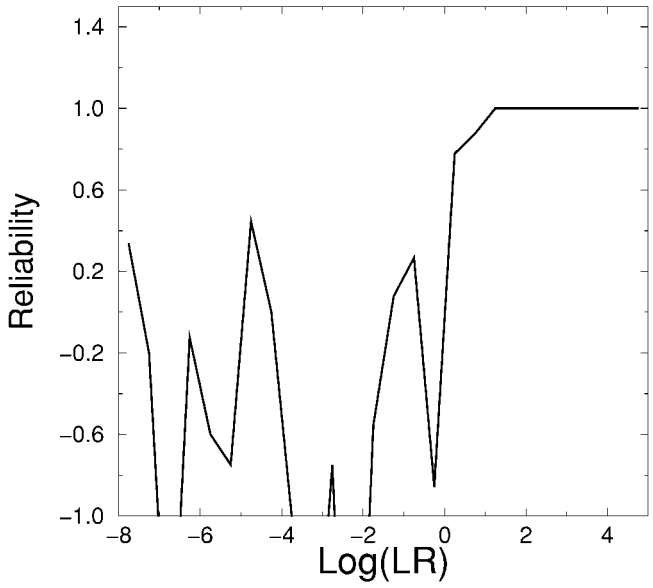

FIG. 6.—Reliability as a function of LR. See eq. (3).

assumption is not valid when the centroid of an extended radio source is used and is further discussed below.

To distinguish between these cases, we compute the likelihood ratio LR_{ij}, defined as

$$\mathrm{LR}_{ij} = \frac{\exp(-r_{ij}^2/2)}{2\pi N(<m_i)\,[(\sigma_{\alpha_i}^2 + \sigma_{\alpha_j}^2)(\sigma_{\delta_i}^2 + \sigma_{\delta_j}^2)]^{1/2}}, \qquad (2)$$

where $N(<m_i)$ is the *local* surface density of objects brighter than candidate *i*. The likelihood ratio LR_{ij} is simply the ratio of the probability of an identification [the Rayleigh distribution: $r\exp(-r^2/2)$] to that of a chance association at r $[2\pi N(<m_i)\sigma_\alpha\sigma_\delta]$. LR_{ij} therefore represents a "relative weight" for each match *ij*, and our aim is to find an optimum cutoff LR_c above which a source is taken to be a reliable and likely candidate. Its advantage over alternative methods (purely based on finding the lowest random chance match; e.g., Downes et al. 1986) is that it allows for a possible distant candidate to still be the "true" identification even when there remains a high chance of it being a spurious background source.

It is important to note that our form for LR_{ij} (eq. [2]) slightly differs from that used by earlier studies (e.g., Lonsdale et al. 1998) in that it does not contain the multiplicative "*Q*" factor in the numerator. This factor represents the a priori probability that a "true" optical counterpart brighter than the flux limit exists amongst the identifications. For our purposes, we will treat LR_{ij} as simply a a relative weight measure for each radio-optical match, just for the purposes of assigning an optimal cutoff for reliable identification (see below). We are not concerned with its absolute value, which is required when computing formal probability measures from LR. For simplicity, we have therefore set $Q = 1$ in this work.

The optical surface density as a function of magnitude to be used in computing LR was determined from the total number of objects visible in our optical frames. The variation in surface density in the vicinity of each radio source caused by possible clustering effects was found to be small: no more than 5% on 2′–3′ scales.

The distribution of LR values for all possible radio source-candidate matches is shown by the shaded histogram in Figure 5. Following Lonsdale et al. (1998), we generate a truly random background population with respect to the radio sources by offsetting the radio source positions by ≈30″. LR values for each radio source were then recomputed, and their distribution is given by the thick-lined histogram in Figure 5. A comparison of the number of associations for (true) radio source positions with the number of associations found for random (offset) positions will enable us to determine a critical value LR_c for reliable identification. From these distributions, we compute the reliability as a function of LR:

$$R(\mathrm{LR}_{ij}) = 1 - \frac{N_{\mathrm{random}}(\mathrm{LR}_{ij})}{N_{\mathrm{true}}(\mathrm{LR}_{ij})}, \qquad (3)$$

where N_{true} and N_{random} are the number of true and random associations, respectively. The reliability computed in this way also represents an approximate measure of the identification probability for a candidate with given LR.

Figure 6 illustrates the reliability as a function of LR. Above

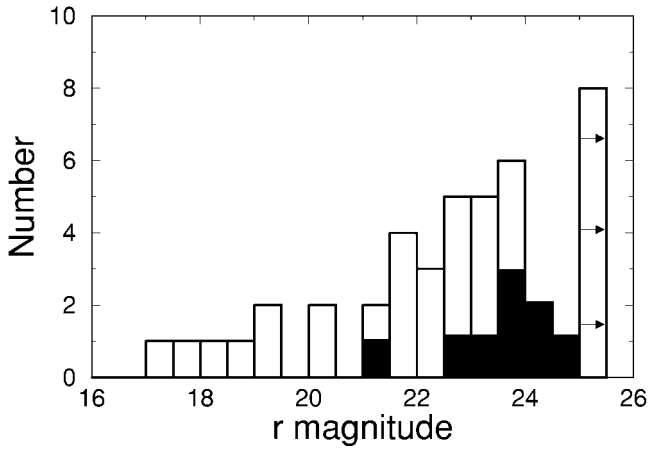

FIG. 7.—Distribution of apparent *r*-band magnitudes for the 26 identified radio sources (*open histogram*) and nine uncertain identifications (*filled histogram*). Eight empty fields are represented by the $r > 25$ mag bin with arrows.

log (LR) ~ 0.5, the reliabilities are ≳85% because few random associations exceed this value of LR (Fig. 5). As a good working measure we therefore assume a cutoff $\log(\mathrm{LR}_c) \simeq 0.5$ above which a source is taken to be a likely candidate. The determination of reliabilities via the LR method is insensitive to variations in $N(< m_i)$ across the field or uncertainties in its derivation, and also the assumption of Gaussian error ellipses in the radio and optical positions. Such uncertainties are "normalized out" when one computes the ratio of random to true number of associations within a search radius when estimating the reliability (eq. [3]). Lonsdale et al. (1998) have shown that the absolute value of LR itself depends on the characteristics of the source population being identified (e.g., stars vs. galaxies). Different populations (assuming they could be classified a priori using some diagnostic) map into different underlying surface densities at the "identifying" wavelength, implying that distributions in LR (eq. [2]) will also be different. For a robust determination of the reliability in such situations, see Lonsdale et al. (1998).

There are two complications to consider in the above method. The first is when one attempts to identify extended (or resolved) radio sources with this method. For all radio sources, we have used the positions of centroids derived from two-dimensional Gaussian fits in computing the LR for optical candidates. For unresolved sources with (Gaussian fitted) sizes ≲15″ (the synthesized FWHP beamwidth), the source is likely to have a compact central component, and the optical position is expected to lie close to its quoted radio centroid. For an extended (resolved) source, however, the radio and optical positions may differ considerably since errors in the radio centroids are only ≲2″. In such cases, if $\mathrm{LR} < \mathrm{LR}_c$, the identification may still be valid, since its low LR value could purely be due to a real large positional offset. The second complication is when a radio source has more than one optical candidate within its search radius with $\mathrm{LR} > \mathrm{LR}_c$. This occurred in about 20% of cases and was primarily due to contaminating stars. We assess these ambiguities and increase the robustness of our identifications by visually examining all optical candidates according to the following criteria:

1. If candidates have $\mathrm{LR} < \mathrm{LR}_c$ for a radio source with $\theta_{\mathrm{min,\,max}} \gtrsim 15''$, then identification is classified as *uncertain*.
2. If candidates have *very low* reliability, $\mathrm{LR} \ll \mathrm{LR}_c$ (for *unresolved* radio sources), or there are no objects in the search radius, then radio source is classified as *empty field*.
3. If $\mathrm{LR} \lesssim \mathrm{LR}_c$, i.e., where reliability is *moderately "low,"* then identification is also uncertain.
4. If more than one optical candidate exists with $\mathrm{LR} > \mathrm{LR}_c$, then only source(s) with extended (galaxy-like) optical profile is (are) taken as the identification. Point sources associated with quasar nuclei are not considered in our identification scheme due to their relatively low surface density compared to galaxies (≈14,000) in sub-mJy radio samples.
5. For unique, $\mathrm{LR} > \mathrm{LR}_c$ candidates, its optical profile is also checked for confirmation.

4.2. Results

Of the 62 radio sources, 43 lie within our optically imaged 27.5 × 27.5 arcmin^2 field. We found optical identifications for 26 to $r \simeq 25$ mag with reliabilities $R_{\mathrm{id}} \gtrsim 80\%$. Four sources have identifications classified as uncertain owing to a moderately low identification reliability of $R_{\mathrm{id}} \lesssim 78\%$ [and $\log(\mathrm{LR}) \lesssim 0.4$]. Five more are uncertain because they have extended radio structure and large possible positional offsets between optical and radio centroid positions. Eight radio sources lie in "definite" optical empty fields with no candidates brighter than $r \simeq 25$ mag.

Other optical follow-up studies found similar results. Georgakakis et al. (1999) identified ≈47% of sources to $R = 22.5$ mag from the Phoenix Deep Survey ($S_{1.4\,\mathrm{GHz}} > 0.2$ mJy) (Hopkins et al. 1998). Deeper identifications of sources as faint as $S_{1.4\,\mathrm{GHz}} \simeq 40$ μJy from Hubble Deep Field images revealed a 80% success rate to $I = 25$ mag (Richards et al. 1999). Ignoring the uncertain identifications in our study (from criteria 1 and 3 above and which are excluded from our analysis), we find that ≈18% of our sources are unidentified to $r \sim 25$. Accounting for differences in bandpasses and sensitivity, this is broadly consistent with the above studies. Figure 7 shows the distribution of apparent magnitude *r* for all reliable (robust) and uncertain identifications in our sample.

4.3. Near-Infrared Data

Near-infrared data in the *J* (1.25 μm), *H* (1.65 μm) and K_s (2.17 μm) photometric bandpasses were obtained from the Two Micron All Sky Survey (2MASS) project database. For multiband detection of point sources, this survey is currently scan-

ning the sky to sensitivities of 16.5, 16.0, and 15.5 mag at signal-to-noise ratios ≈7, ≈5, and ≈7, respectively, in *J*, *H*, and K_s. The data relevant to this study are not yet released in the public catalogs and were retrieved from the "internal working database" at IPAC.[6] Photometry in this database was determined using custom PSF-fitting software, and algorithms are described in the Explanatory Supplement to the 2MASS Second Incremental Data Release (R. Cutri et al. 2000).[7] Since such data have not been subjected to the same rigorous quality assurance as that in the public release catalogs, we have examined individual images for quality and any possible systematic uncertainties in the photometry.

To maximize the possible number of detections, we searched for near-IR counterparts to each radio source with a conservatively low signal-to-noise ratio threshold of ∼5 in each band. In cases where a source was detected in only one or two of the three bandpasses, *J*, *H*, and K_s, we note its "band-filled" 95% confidence upper limit in the undetected band. In other words, the 2MASS catalog also reports upper limits to measurements in an undetected band by placing an aperture over the position inferred from detections in other bands. The image pixel scale of the 2MASS detectors is 2.″0, and the positional uncertainties are ≲0.″5. Owing to the relatively shallow flux limits of the 2MASS survey, the background source surface density is low enough that chance associations with radio positions are very unlikely.

We searched the 2MASS database for near-IR counterparts to our 43 radio sources that have *available optical* information from our deep optical survey and examined their images for quality. We found seven reliable matches with six detections in *J*, seven in *H*, and four in K_s at the ≳5 σ level. Upper limits were available for the remaining "band-filled" values.

Results of our optical identification analysis and available near-IR data are shown in Table 3. In column order, this table reports (1) the radio source name (see Table 2); (2) R.A.(J2000) and (3) decl.(J2000) of the optical counterpart of the radio source; (4) optical-radio position separation ($\delta_{\rm rad\text{-}opt}$) in arcseconds; (5) logarithm of the likelihood ratio, log (LR); (6) reliability of the optical identification (see eq. [3]); (7) apparent *r*-band magnitude; (8) *J*, (9) *H*, and (10) K_s magnitudes with errors or 2 σ upper limits; (11) $r-H$ color; (12) $r-K_s$ color; and (13) the optical morphology if the optical counterpart is visually resolved with size $\gtrsim 5\theta_{\rm FWHM}$(PSF).

Optical morphologies were determined from light profile fitting of individual sources and comparison with $R^{1/4}$-law (elliptical-like) and exponential (disklike) profiles. In cases where a disturbed or interacting morphology is apparent, then it is designated to have an irregular (labeled as "Irr") morphology. Sources unresolved in the optical with typically $\lesssim 5\theta_{\rm FWHM}$(PSF) are designated as "unknown" and labeled as "?" in Table 2.

4.4. Optical and Radio Map Overlays

InFigure 8 we show the optical image+radio map overlays for the 43 radio sources with available optical information. A visual inspection of the optical images of resolved counterparts shows a diverse morphological mix, consistent with previous studies. About 40% of our optical identifications have elliptical/disklike morphology, while ∼10% can be identified as exhibiting peculiar (either interacting or disturbed) morphologies. It is important to note that these "disturbed" sources are based on visual inspection alone, and their morphology could still be uncertain until future spectroscopy confirms their nature. The elliptical/disk hosts also tend to be associated on average with sources of relatively brighter radio flux density (≳2 mJy) than the irregular class. This is consistent with previous radio-optical identification studies which find an increasing fraction of irregular-type galaxies at $S_{1.4} \lesssim 2$ mJy (e.g., Kron et al. 1985; Hammer et al. 1995; Gruppioni et al. 1999) and a significant number of elliptical galaxies hosting the brighter extended radio galaxies and AGNs (Condon 1989).

A further observation is the unique radio structure exhibited by our eight optical empty field sources with $r > 25$ mag. These are represented by maps in Figure 8 labeled by the letter "E." All show compact and symmetric (presumably unresolved) structures and could represent either of the following: distant (possibly dusty) AGNs where with our radio sensitivity we could have detected a nominal FR I galaxy to $z \sim 1.3$; or nearby, compact dusty starbursts at $z \lesssim 0.3$ as constrained by typical starburst luminosities, $L_{1.4\,\rm GHz} \lesssim 10^{23}$ W Hz^{-1}. The second explanation for the nature of the empty fields is more plausible, given that the majority of sub-mJy radio sources are associated with star-forming galaxies and less than 5% are usually identified with bright FR I galaxies at $z \lesssim 1$ (Kron et al. 1985).

5. ANALYSIS OF RADIO AND OPTICAL–NEAR-INFRARED COLORS

This section presents an analysis of flux ratios between the radio, near-IR, and optical bands to explore possible contributions from AGNs and starbursts to the observed radio emission as well as the importance of absorption by dust. Because we lack spectroscopic information, our analysis treats the sub-mJy sources as one homogeneous population and uses a simple stellar synthesis model to interpret its properties quantitatively.

5.1. A Simple Synthesis Model

We can predict the radio–optical(–near-IR) flux ratios and $r-K$ colors for a range of galaxy types using the stellar population synthesis code of Bruzual & Charlot (1993). On its own however, the Bruzual & Charlot model does not directly predict

[6] The Infrared Processing and Analysis Center, California Institute of Technology.

[7] R. Cutri et al. 2000, Explanatory Supplement to the 2MASS Second Incremental Data Release (http://www.ipac.caltech.edu/2mass/releases/second/doc/explsup.html).

TABLE 3
OPTICAL-INFRARED DATA

Name (1)	R.A.[a] (J2000) (2)	Decl.[a] (J2000) (3)	$\delta_{rad-opt}$ (arcsec) (4)	log (LR) (5)	R_{id}[e] (6)	r (7)	$J(\sigma_J)$[b] (8)	$H(\sigma_H)$ (9)	$K(\sigma_K)$ (10)	$r-H$ (11)	$r-K$ (12)	Morphology[c] (13)
RAD J001216+2601[d]	00 12 16.530	+26 01 32.77	7.41	−4.163	≪0.1	24.083(?)	…	…	…	…	…	?
RAD J001216+2543	00 12 16.783	+25 43 01.34	1.31	3.537	≈1	17.565	16.056(0.093)	15.409(0.138)	14.525(0.086)	2.156	3.040	E
RAD J001217+2602	00 12 17.280	+26 02 54.85	1.78	1.514	≈1	22.057	…	…	…	…	…	E
RAD J001218+2554	…	…	…	…	…	>25	…	…	…	…	…	…
RAD J001227+2543	00 12 27.033	+25 43 41.19	3.09	0.685	0.862	22.971	…	…	…	…	…	Irr
RAD J001237+2607	00 12 37.248	+26 07 48.49	0.39	2.883	≈1	19.371	…	…	…	…	…	S
RAD J001242+2600[d]	00 12 42.347	+26 00 30.83	3.42	0.278	0.783	23.621(?)	…	…	…	…	…	?
RAD J001243+2558	…	…	…	…	…	>25	…	…	…	…	…	?
RAD J001246+2543	00 12 45.777	+25 43 50.59	3.83	1.293	≈1	21.169	…	…	…	…	…	E
RAD J001247+2602[d]	00 12 47.889	+26 02 35.96	4.03	0.302	0.788	22.768(?)	…	…	…	…	…	E
RAD J001250+2550	00 12 50.137	+25 50 10.86	1.52	1.225	0.995	23.128	…	…	…	…	…	E
RAD J001252+2549	00 12 51.969	+25 49 38.81	0.65	2.919	≈1	18.984	17.416(0.285)	16.057(0.204)	>16.321	2.927	<2.663	E
RAD J001254+2600[d]	00 12 54.855	+26 00 44.70	3.83	0.246	0.764	23.004(?)	…	…	…	…	…	?
RAD J001255+2541[d]	00 12 55.064	+25 41 54.13	4.56	−0.689	≪0.1	23.599(?)	…	…	…	…	…	?
RAD J001257+2559	00 12 57.287	+25 59 43.60	0.03	2.248	≈1	20.384	17.066(0.210)	16.131(0.225)	>15.178	4.253	<5.206	S
RAD J001259+2607	00 12 59.187	+26 07 19.09	1.21	2.706	≈1	19.010	15.158(0.074)	14.290(0.075)	13.913(0.074)	4.720	5.097	S
RAD J001300+2556	00 13 01.007	+25 56 57.08	0.35	1.505	≈1	22.974	…	…	…	…	…	Irr
RAD J001303+2602	00 13 03.204	+26 02 07.27	0.31	1.681	≈1	22.492	…	…	…	…	…	E
RAD J001304+2544	…	…	…	…	…	>25	…	…	…	…	…	?
RAD J001305+2607	00 13 05.293	+26 07 53.81	1.60	1.675	≈1	21.835	>16.403	16.118(0.207)	>14.996	5.717	<6.839	E
RAD J001307+2542	…	…	…	…	…	>25	…	…	…	…	…	…
RAD J001311+2556	00 13 11.603	+25 56 41.19	1.95	1.515	≈1	21.950	…	…	…	…	…	Irr
RAD J001313+2545	00 13 13.049	+25 45 17.44	2.33	0.778	0.882	23.464	…	…	…	…	…	?
RAD J001314+2541	00 13 14.595	+25 41 14.73	0.78	1.118	0.967	23.698	…	…	…	…	…	?
RAD J001318+2604C1	00 13 18.794	+26 04 37.24	1.64	1.189	0.984	22.847	…	…	…	…	…	Irr
RAD J001320+2604C2	00 13 20.199	+26 04 10.69	1.37	1.706	≈1	21.938	…	…	…	…	…	E
RAD J001320+2556	00 13 20.705	+25 56 53.85	2.88	1.647	≈1	20.481	…	…	…	…	…	E
RAD J001321+2543	00 13 21.339	+25 43 48.81	1.15	0.996	0.936	22.929	16.206(0.104)	15.536(0.128)	15.224(0.179)	7.393	7.705	?
RAD J001323+2600[d]	00 13 23.256	+26 00 27.73	4.28	0.247	0.775	24.040(?)	…	…	…	…	…	?
RAD J001325+2553	00 13 25.803	+25 53 39.14	2.75	0.695	0.864	23.650	…	…	…	…	…	?
RAD J001327+2543	00 13 27.260	+25 43 33.55	1.58	1.265	≈1	22.639	…	…	…	…	…	E
RAD J001339+2543	…	…	…	…	…	>25	…	…	…	…	…	…
RAD J001342+2546[d]	00 13 41.666	+25 46 16.96	8.27	0.238	0.770	21.194(?)	…	…	…	…	…	Irr
RAD J001350+2608	00 13 50.572	+26 08 12.05	4.73	0.617	0.858	22.178	…	…	…	…	…	E
RAD J001355+2553	00 13 55.857	+25 53 28.22	0.75	3.729	≈1	17.286	15.642(0.071)	14.756(0.082)	14.419(0.098)	2.530	2.867	E
RAD J001359+2601	…	…	…	…	…	>25	…	…	…	…	…	…
RAD J001359+2605[d]	00 13 59.795	+26 05 22.01	4.84	−0.760	≪0.1	23.763(?)	…	…	…	…	…	?
RAD J001401+2559C1	00 14 01.559	+25 59 57.15	2.31	0.861	0.903	23.390	…	…	…	…	…	?
RAD J001403+2559C2[d]	00 14 03.088	+25 59 33.06	4.20	−0.790	≪0.1	24.707(?)	…	…	…	…	…	?
RAD J001405+2551	00 14 05.728	+25 51 28.88	1.16	1.893	≈1	21.508	…	…	…	…	…	E
RAD J001408+2550	…	…	…	…	…	>25	…	…	…	…	…	…
RAD J001411+2546	…	…	…	…	…	>25	…	…	…	…	…	…
RAD J001411+2541	00 14 11.805	+25 41 22.34	1.93	1.016	0.938	23.164	…	…	…	…	…	?

NOTE.—Units of right ascension are hours, minutes, and seconds, and units of declination are degrees, arcminutes, and arcseconds.
[a] Refers to optical position.
[b] Values with ">" are 2 σ upper limits on measured fluxes; otherwise, errors are quoted in parentheses.
[c] Optical morphology: E, elliptical; Irr, irregular or disturbed; S, spiral; ?, unknown.
[d] Optical identification is uncertain because of either extended radio emission and large offset from radio centroid position or "moderately low" LR value.
[e] Reliability of the optical identification. Cases with "very low" and "very large" log (LR) are listed with $R_{id} \ll 1$ and $R_{id} \approx 1$, respectively.

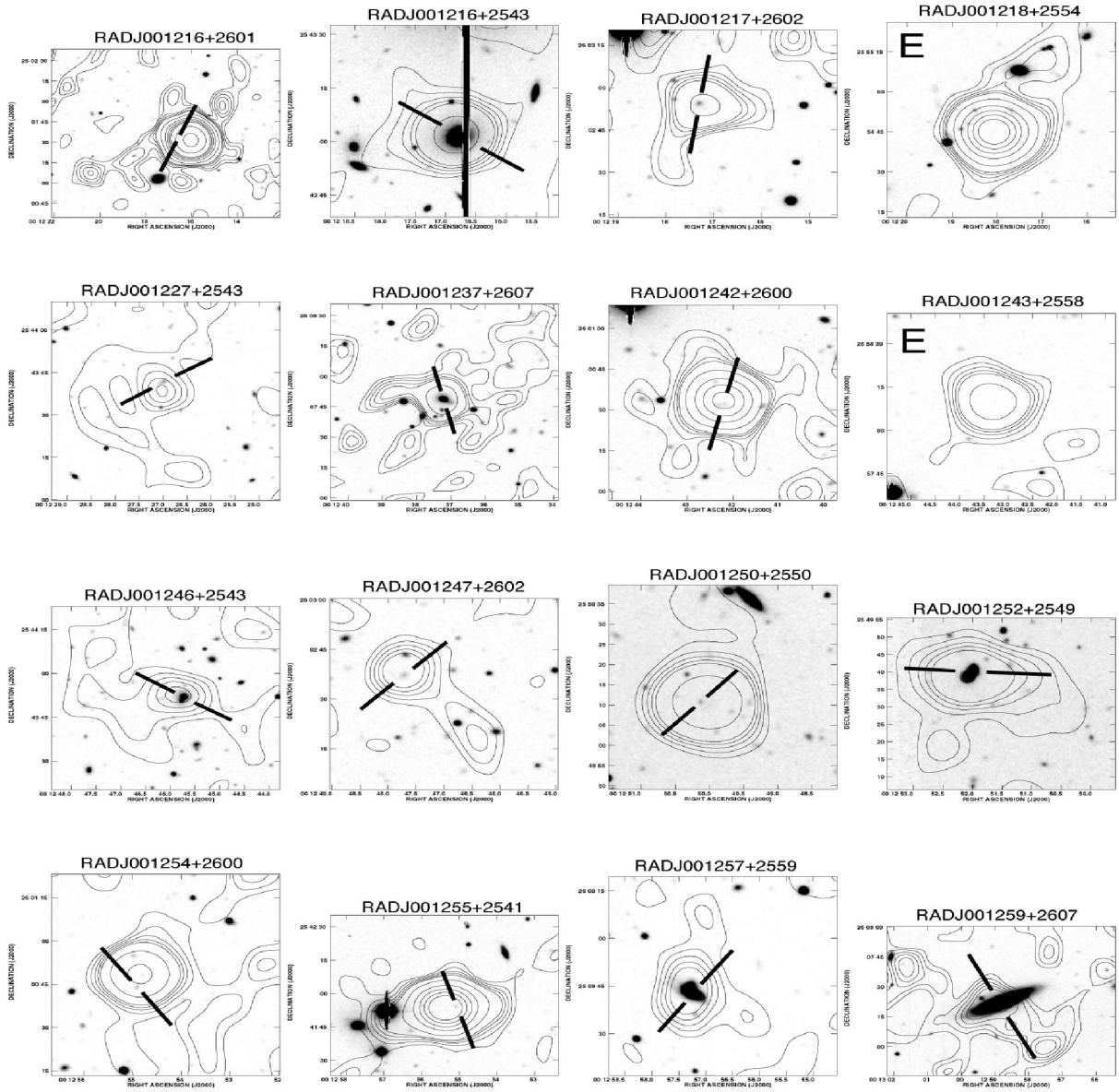

FIG. 8.—Optical image (*r*-band) and radio contour overlays for the 43 sources with available optical information. Contour levels are 1, 2, 3, 4, 5, 10, 20, 30, 40, 50, 100, and 200 σ, where σ refers to the local rms noise (see Table 1). Optical candidates are indicated within broken lines—see Table 3 for reliability estimates. Maps labeled with "E" in upper left corner represent optical empty fields.

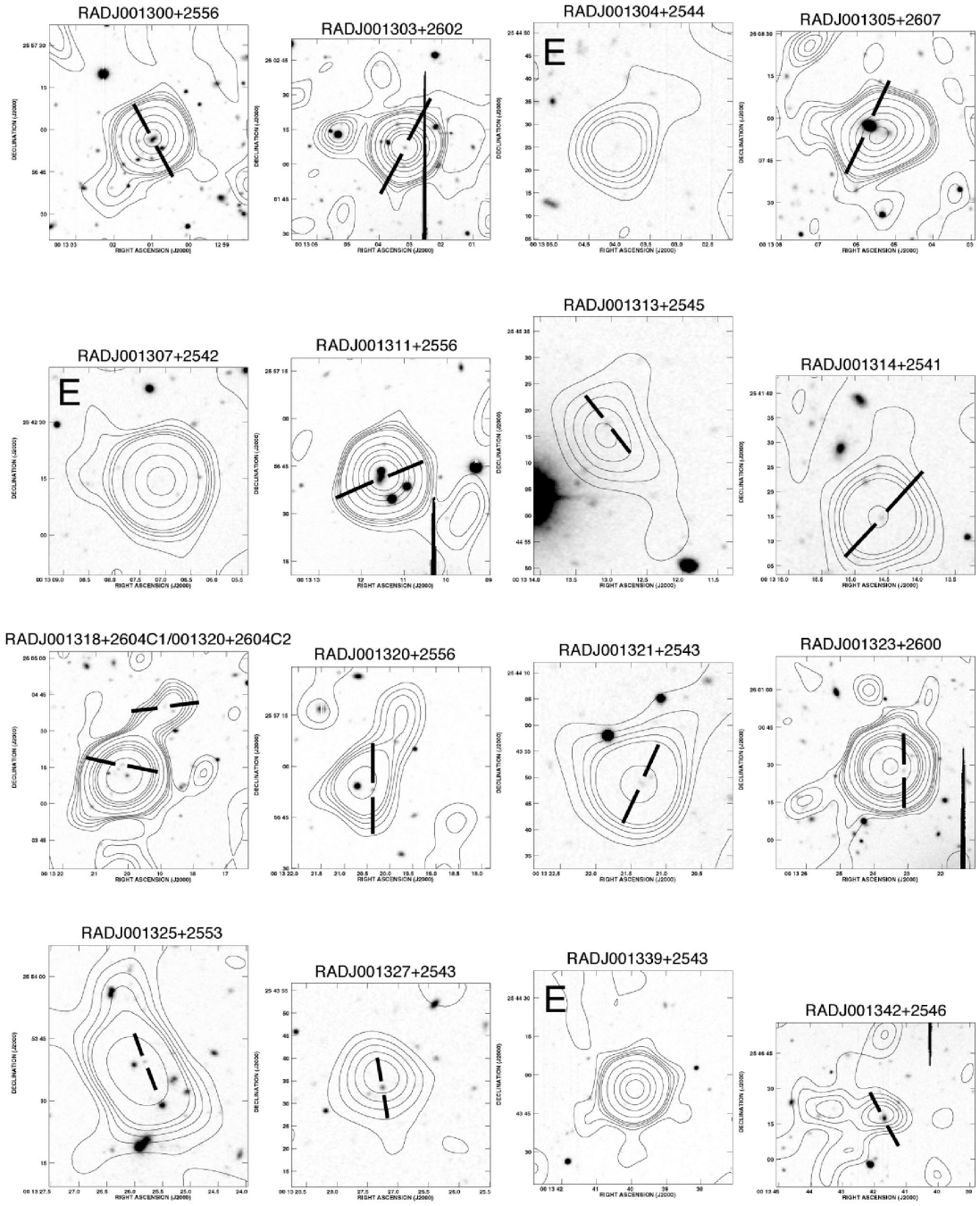

FIG. 8.—*Continued*

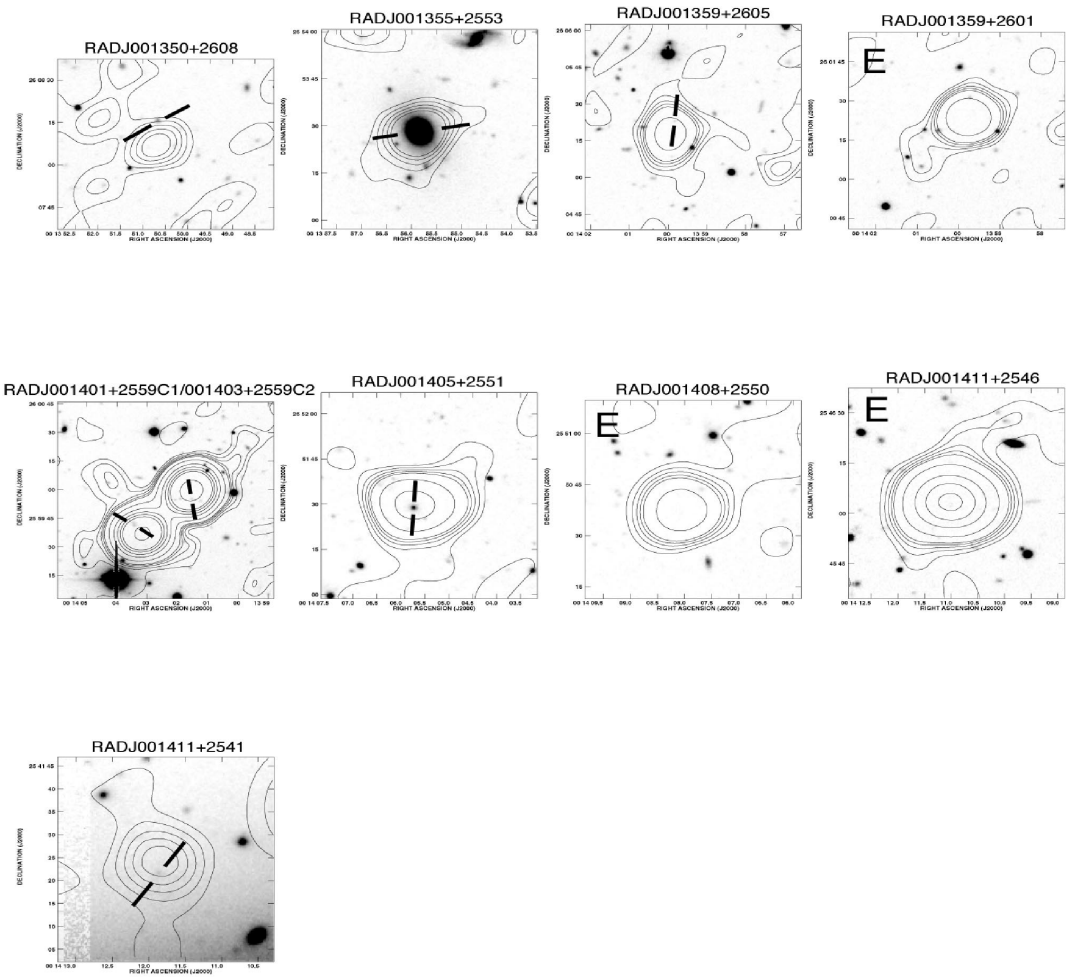

FIG. 8.—*Continued*

the amount of radio emission expected from a star-forming galaxy, which we need for the determination of flux ratios involving the radio band. We do this by relating the star formation rates derived from empirical calibrations involving the UV and radio bands as follows.

The 1.4 GHz radio emission from star-forming systems is believed to be primarily synchrotron emission from cosmic rays accelerated in supernova remnants plus a small (~10%) thermal contribution from H II regions (Condon & Yin 1990; Condon 1992). Thus, to a good approximation, the radio luminosity is taken to be proportional to the formation rate of stars with $M > 5\ M_{\odot}$:

$$\mathrm{SFR}(M \geq 5\ M_{\odot}) = \frac{L_{1.4\,\mathrm{GHz}}}{4 \times 10^{28}\ \mathrm{ergs\ s^{-1}\ Hz^{-1}}}\ M_{\odot}\ \mathrm{yr}^{-1} \quad (4)$$

TABLE 4
POPULATION SYNTHESIS MODELS

Type	SFR(t)	IMF	Age[a] (Gyr)
E/SO	$\tau_1^{-1} \exp(-t/\tau_1)$	Scalo	12.7
Sab/Sbc	$\tau_8^{-1} \exp(-t/\tau_8)$	Scalo	12.7
Scd/Sdm	Constant	Salpeter	12.7
SB	Constant	Salpeter	0.1

[a] For the SB type, an age of 0.1 Gyr is assumed to apply at all redshifts. For other types, this refers to the present-day age.

(Condon 1992). These same massive stars will also contribute significantly to the UV continuum emission in the range ~1200–2500 Å. In particular, there have been many different calibrations of the SFR from the UV flux. For a Salpeter initial mass function (IMF) from $m\ M_\odot$ to 100 $M_\odot$, the calibration of Madau, Pozetti, & Dickinson (1998) (which assumes *no dust* correction) yields

$$\mathrm{SFR}(M \geq m\ M_\odot) = Q_m \left(\frac{L_{\mathrm{UV}}}{7.14 \times 10^{27}\ \mathrm{ergs\ s^{-1}\ Hz^{-1}}} \right)\ M_\odot\ \mathrm{yr}^{-1}. \quad (5)$$

We have modified the initial relation of Madau et al. (1998) to include the factor Q_m, which represents the fraction of stellar masses contributing to the observed SFR,

$$Q_m = \frac{\int_{m\,M_\odot}^{100\,M_\odot} M\psi(M)dM}{\int_{0.1\,M_\odot}^{100\,M_\odot} M\psi(M)dM}, \quad (6)$$

where $\psi(M) \propto M^{-x}$ is the IMF. For $m = 0.1$, we have $Q_m = 1$. Assuming a Salpeter IMF ($x = 2.35$), we find that for stars with $M > 5\ M_\odot$, $Q_m \simeq 0.18$. With this fraction, and equating the two SFR calibrations (eqs. [4] and [5]), we find that the luminosity densities at 1.4 GHz ($L_{1.4\,\mathrm{GHz}}$) and ≃2100 Å (L_{UV}) are very nearly equal. We therefore assume that the rest-frame 1.4 GHz flux density is directly given by the flux density at ≃2100 Å as specified by the synthesized model spectrum. In general terms, the observed radio flux (in the same units as the synthesized UV spectrum) can be written

$$f_\nu(1.4\ \mathrm{GHz})_{\mathrm{obs}} = (1+z)^{1-\alpha} f_\nu(2100\ \text{Å})_{\mathrm{rest}}, \quad (7)$$

where $\alpha \simeq 0.8$ is the radio spectral index (Condon 1992) and $f_\nu(2100\ \text{Å})_{\mathrm{rest}}$ is the rest-frame (unreddened) UV spectral flux. We must emphasize that this relative radio flux is only that associated with the star formation process. Possible additional contributions, such as contaminating AGNs, are not considered in this model.

We calculated flux ratios involving the radio, near-IR, and optical bands using evolutionary synthesis models for ellipticals (E/SO), early- (Sab/Sbc) and late- (Scd/Sdm) type spirals, and "very blue" starbursts (SB). These are meant to represent the possible contributions to the sub-mJy radio sources, and each class is defined by a characteristic star formation rate as a function of time. As supported by local observations (e.g., Gavazzi & Scodeggio 1996), we assumed that E/SO and Sab/Sbc galaxies have an exponentially decaying SFR of the form $\psi(t) \propto \tau^{-1} \exp(-t/\tau)$, where τ is the e-folding time. Values of $\tau = 1$ and $\tau = 8$ Gyr were adopted for the E/SO and Sab/Sbc galaxies, respectively. For late-type spirals (Scd/Sdm) and young starbursts (SB), we assumed constant SFRs with different ages. All models used to generate the spectral energy distributions (SEDs) are summarized in Table 4. The models assume $H_0 = 50$ km s^{-1} Mpc^{-1}, $q_0 = 0.5$, and a galaxy formation redshift $z_f = 10$, which corresponds to an age of 12.7 Gyr at $z = 0$.

To explore the effects of dust on our flux ratios and colors, each model SED was reddened in the source rest frame with an extinction curve $\xi(\lambda) \equiv A_\lambda/A_V$ characteristic of the Small Magellanic Cloud (SMC), which appears to be a good approximation for the ISM of nearby galaxies (Calzetti, Kinney, & Storchi-Bergmann 1994). This approximation is most accurate for the reddest wavelengths of starburst galaxy spectra (7000 Å–3 μm), although it breaks down severely at $\lambda \lesssim 2500$ Å (Calzetti et al. 2000). We have used the analytical fit for $\xi(\lambda)$ as derived by Pei (1992) for the SMC. For simplicity, we assumed that the dust is distributed in a homogeneous foreground screen at the source redshift.

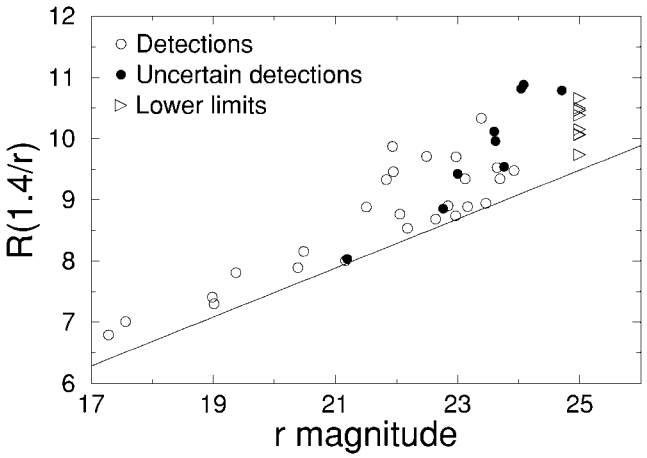

FIG. 9.—Radio-optical (r-band) flux ratio (see eq. [8]) as a function of r magnitude for all radio sources with available optical information. For the observed range of r magnitudes, the solid line represents the prediction at the limiting flux of the survey, $S_{1.4\,\mathrm{GHz}} \approx 0.3$ mJy.

5.2. Data and Model Comparisons

In Figure 9 we plot the radio-optical flux ratio, $R(1.4/r)$, defined as

$$R(1.4/r) = \log(S_{1.4}/\mathrm{mJy}) + 0.4r, \quad (8)$$

where $S_{1.4}$ and r are the radio flux and optical r-band magnitude,

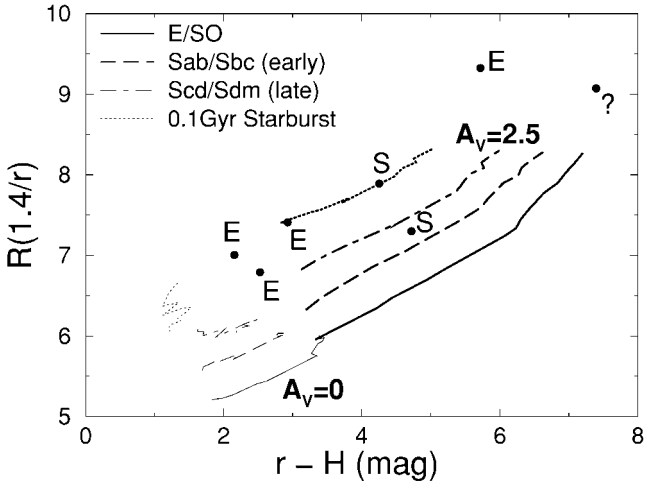

FIG. 10.—Radio-optical (*r*-band) flux ratio (see eq. [8]) as a function of $r-H$ color for radio sources with available optical and near-IR detections. The predictions of four synthesis models for $0 \le z \le 1.5$ (*from bottom left to top right*) are also shown. These assume no extinction (*thin curves*) and with a rest-frame extinction $A_V = 2.5$ mag (*thick curves*).

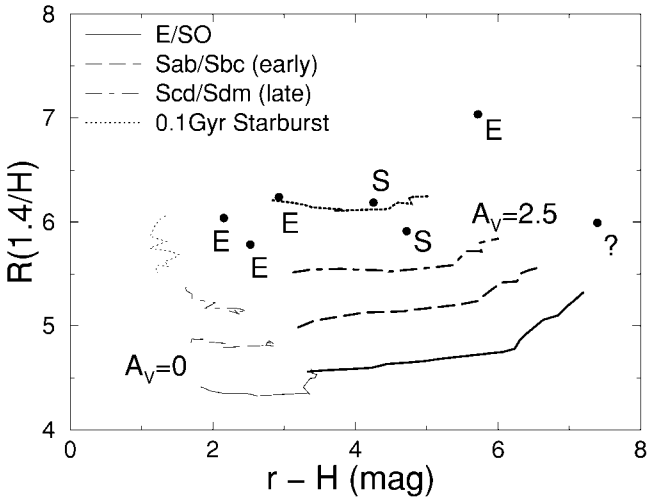

FIG. 11.—Radio–near-IR (*H*-band) flux ratio as a function of $r-H$ color and models which include no extinction (*thin curves*) and $A_V = 2.5$ mag (*thick curves*).

respectively. The distribution seen in observed values of $R(1.4/r)$ is larger at the faintest optical magnitudes $r > 21.5$. However, there are few galaxies with $r < 21.5$; nonetheless, the scatter at $r > 21.5$ is consistent with that found at $r \lesssim 19$ in a larger follow-up study of sub-mJy radio sources by Georgakakis et al. (1999).

Figure 10 shows $R(1.4/r)$ as a function of $r-H$ color for all sources with available optical and near-IR data. Our reason for using $r-H$ color is that the *H* band yielded more "definite" detections than the other near-IR bandpasses. Although the numbers are still relatively small, this facilitates the best comparison with the synthesis models. The predictions for four galaxy types (see Table 4 and § 5.1) are shown for no dust reddening (*thin curves*) and a rest-frame extinction $A_V = 2.5$ mag. The morphological mix of data shows a relatively large dispersion in $r-H$ color that is more consistent with the range predicted by the models that *include dust*. This suggests that on average, the optical–near-IR continua of most sources in Figure 10 are reddened by a uniform (possibly "optically thin") dust component with $A_V \simeq 2$–2.5 mag absorption. This measure is consistent with spectroscopic studies of nearby starbursts by Calzetti, Kinney, & Storchi-Bergmann (1996) and Meurer et al. (1997) and photometric modeling by Nakata et al. (1999).

We must emphasize that our models account only for radio emission produced from star formation processes. The sources labeled as elliptical (or early type) in Figure 10 are not expected to lie on any of the star formation derived loci. An AGN most likely dominates their radio emission. We include them here merely for comparison, and their relationship to normal starbursts is discussed further below.

The sources in Figure 10 appear more-or-less consistent with the dusty "0.1 Gyr starburst" model. This could in principle apply to the two sources with spiral/disklike morphology (labeled "S"), but is unconventional for the five elliptical morphologies (see below). A comparison with radio–near-IR flux ratios further constrains the underlying properties of these sources. Figure 11 shows the radio–near-IR flux ratio $R(1.4/H)$, defined analogous to equation (8), as a function of $r-H$ color. The near-IR emission is dominated by old stars and is less affected by dust than the optical. The radio–near-IR flux ratio should therefore be relatively insensitive to dust. Given the simplicity of our models, the two disklike sources may not necessarily represent "0.1 Gyr starbursts" as indicated in Figure 11. They could also belong to the Sab/Sbc or Scd/Sdm classes. For this to be true, the following additional components may play an important role in more "realistic" models: "optically thick" dust that *completely obscures* both the *H* and *r* emission without causing appreciable reddening in $r-H$ color, or contamination by at least an order of magnitude times more radio emission from a central AGN than that produced purely by supernovae. The second possibility is favored by radio observations of a number of luminous infrared galaxies by Norris, Allen, & Roche (1988), where some showed evidence for significant radio emission from compact Seyfert-like nuclei.

The large discrepancy between the four sources with elliptical morphologies (labeled "E") and predictions from the early-type E/SO models suggests the importance of a significant AGN contribution to the radio emission. Appreciable amounts of optically thick dust suppressing the optical and near-IR light (except for extinction by diffuse, optically thin dust) is not favored by observations (e.g., Goudfrooij & de Jong 1995). Most, if not all, of these ellipticals are likely to be radio powered by AGNs. At the limiting sensitivity of our radio survey ($\simeq$0.3 mJy), a nominal FR I galaxy (with $L_{1.4} = 10^{24}$ W Hz^{-1}) could be detected to $z \simeq 1.3$, and indeed the spread in $r-H$ color for the ellipticals in Figure 11 is consistent

with the E/SO (optically thin dust) model to this redshift. A comparison of model $R(1.4/H)$ values with actual observed values implies that such AGNs will contribute a factor of 10^2 times more radio emission than that produced by any underlying star formation activity in these systems. It is important to note that the ratio of AGN to stellar powered radio activity has a huge spread for the elliptical population in general and that the factor of 10^2 only illustrates a property specific to the ellipticals in our radio sample.

To summarize, our use of a simple synthesis model that includes radio emission and dust reddening to analyses the properties of sub-mJy radio sources has shown the following: first, the presence of dust with extinctions $A_V \simeq 2$ mag and possibly greater, consistent with previous more direct determinations, and second, that the level of radio emission from nonstellar processes such as AGNs could be easily inferred and constrained. This will be particularly important for starbursts hosting Seyfert nuclei where a comparison with more sophisticated dust models may be required to infer the relative contributions.

6. A METHOD TO SELECT "ULIGs" VIA RADIO-OPTICAL COLOR

Since the emission (and dust absorption) properties from normal galaxy populations are reasonably well known, a color-color diagram such as Figure 10 could provide a potential diagnostic for selecting ultraluminous infrared galaxies (ULIGs) to high redshift. The relatively low sensitivity of *IRAS* has primarily confined ULIG selection to the local universe (Sanders & Mirabel 1996), although there is some speculation that recently discovered faint "SCUBA" sources at submillimeter wavelengths could represent their high-redshift counterparts (e.g., Blain et al. 1999). Approximately 80% of local ULIGs are believed to be powered by starbursts, and the remainder show evidence for an AGN contribution (Genzel et al. 1998; Lutz et al. 1998). Far-infrared observations have shown that dust and molecular gas in local ULIGs is concentrated in compact regions $\lesssim$1 kpc (Okumura et al. 1991; Bryant 1996) and that a large fraction of the optical-UV emission is hidden by optically thick dust (Sanders et al. 1988). A study of their properties and importance to galaxy evolution therefore requires observations at wavelengths virtually immune to dust absorption. Radio frequencies provide an excellent window of opportunity.

Figure 12 illustrates the predicted locus in color-color space using the synthetic SEDs of three local far-IR–selected systems: Arp 220 ($L_{\rm IR} \simeq 1.6 \times 10^{12}\ L_\odot$), a ULIG undergoing a powerful starburst as seen via high-resolution radio observations by Smith et al. (1998); M82 ($L_{\rm IR} \simeq 6 \times 10^{10}\ L_\odot$), a system undergoing a weak-to-moderate starburst; and Mrk 273 ($L_{\rm IR} \simeq 2.6 \times 10^{12}\ L_\odot$), a ULIG whose bolometric emission is believed to be dominated by a hidden central AGN from the presence of strong Seyfert 2 lines and moderately strong hard

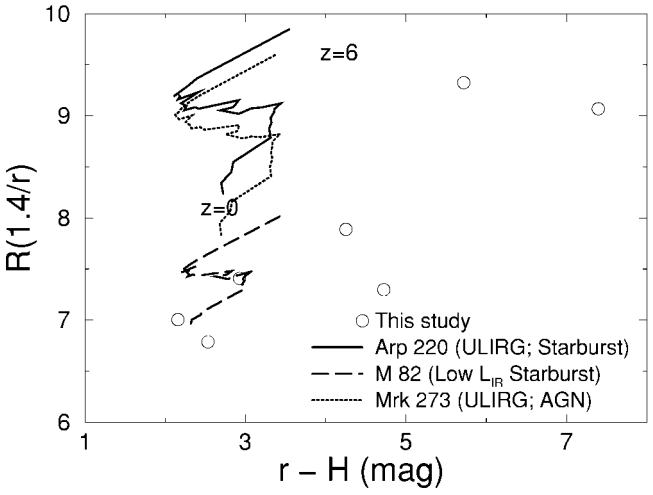

FIG. 12.—Locus of observed radio-optical flux ratio vs. $r-H$ color for $0 \le z \le 6$ ($\Delta z = 0.2$) using three local far-IR–selected systems: Arp 220 ($L_{\rm IR} \simeq 1.6 \times 10^{12}\ L_\odot$; strong starburst), M82 ($L_{\rm IR} \simeq 6 \times 10^{10}\ L_\odot$; weak/moderate starburst) and Mrk 273 ($L_{\rm IR} \simeq 2.6 \times 10^{12}\ L_\odot$; AGN dominated).

X-ray (2–10 keV) emission (Turner et al. 1997). We have used the synthetic SEDs generated by Devriendt, Guiderdoni, & Sadat (1999) to model the starburst emission. These authors used a self-consistent modeling approach to predict the stellar optical–UV–near-IR emission, its reprocessing into the mid-IR–submillimeter by dust, and the nonthermal stellar-powered radio emission based on the empirical radio–far-IR luminosity correlation. Because of its strong AGN-dominated nature, the starburst synthetic SED predicted by Devriendt et al. for Mrk 273 differs appreciably from that observed in the *radio*. For this source, we therefore used the Devriendt et al. SED at wavelengths $\lambda < 1$ mm and extrapolated into the radio using its actual *observed* radio–to–1 mm spectral slope and fluxes (obtained from the NASA/IPAC Extragalactic Database[8]).

Figure 12 shows that a galaxy characteristic of the (low-IR luminous) M82 system will occupy a region similar to that occupied by normal galaxies in this study (and also their predicted synthetic colors in Fig. 10). However, luminous systems classified as ULIGs (Arp 220 and Mrk 273) will tend have higher radio-optical flux ratios which could be easily selected. This can be explained by the well-observed correlation between far-IR luminosity and far-IR (60–100 μm)–optical spectral slope (Soifer et al. 1987). Consequently, the most IR-luminous systems with the largest far-IR–optical ratios are also likely to have a high level of radio emission owing to its strong correlation with IR luminosity. This will lead to a larger than average radio-optical flux ratio for ULIGs in general as shown in Figure 12.

[8] The NASA/IPAC Extragalactic Database (NED) is operated by the Jet Propulsion Laboratory, California Institute of Technology, under contract with the National Aeronautics and Space Administration.

The existence of systems with either larger rest-frame optical-UV extinction or excess AGN contribution to the radio than the ULIGs considered here will be shifted further upward on this plot. Diagnostics to distinguish between AGN- and starburst-dominated ULIGs using radio-optical color alone will not be trivial and is left to a future study. The three ULIGs in Figure 12 represent a range of known ULIGs and their location on this plot simply serves as a diagnostic to preselect ULIG candidates for further study.

A system like Arp 220 [with $\nu L_{\nu}(1.4\ \mathrm{GHz}) \simeq 2.5 \times 10^6\ L_{\odot}$] could be observed to redshift $z \sim 1.6$[9] if initially selected from a radio survey limited to $S_{1.4\,\mathrm{GHz}} \simeq 50\ \mu$Jy. Thus, to limiting sensitivities reached by existing 1.4 GHz surveys, such a method may not probe the highest redshifts. Nonetheless, as shown in Figure 12, such systems could still be well separated from normal galaxies to this redshift. Assuming an Arp 220–like SED and moderate luminosity evolution [$L_{60\,\mu\mathrm{m}} \propto (1+z)^{2.5}$], the surface density of ULIGs to $z \sim 1.6$ is expected to be of order 150 deg^{-2} at $S_{1.4\mathrm{GHz}} \gtrsim 50\ \mu$Jy, or about 6% of the integral count to this sensitivity (Richards 2000). They should therefore exist in significant numbers in deep large-area radio surveys.

7. SUMMARY AND CONCLUSIONS

We have used the VLA radio telescope to image a contiguous 33×33 arcmin^2 area to a (mean) limiting (5 σ) sensitivity of $\simeq$0.35 mJy. From a total of 62 detections, the results of optical and near-IR photometry are reported for 43 sources. Our optical photometry is more sensitive than previous optical follow-up studies of radio surveys of similar depth. Our main findings are the following:

1. We have used a robust likelihood ratio method for determining optical identifications and their reliability. This method is seldom used in identification studies and is insensitive to assumptions concerning fluctuations in background source density and Gaussian error distributions. We assigned optical candidates to 26 radio sources with reliability $\gtrsim$80%. Nine radio sources are uncertain and/or ambiguous, and eight are empty fields. Near-infrared photometry from the 2MASS database was reported for seven sources.

2. The eight optical empty field sources all display compact and symmetric radio morphologies and most probably represent compact starbursts at $z \lesssim 0.3$ strongly obscured by dust. They may require at least 4 mag of optical extinction to account for their large radio-optical flux ratio compared to the identified population. Our conclusion for them being "compact starbursts" is very tentative as it is purely based on starburst versus AGN number statistics expected from sub-mJy radio surveys. Further deep infrared-optical imaging and spectroscopy will be necessary.

3. Consistent with previous studies, our deep ($r \simeq 25$) optical imaging shows that the optical appearance can be divided into two classes according to radio flux density: elliptical-like morphologies for $\gtrsim$2 mJy, and peculiar or disturbed for $\lesssim$2 mJy.

4. Using a stellar synthesis model which includes radio emission and dust reddening, we find that the near-IR–optical emission in a small, bright subsample is reddened by "optically thin" dust with $A_V \simeq 2$–2.5 mag, regardless of morphological type. This appears consistent with other more direct determinations. Consistent with previous studies, the radio emission from early-type systems seems to be powered by AGNs rather than star formation to account for their anomalously large radio–optical(–near-IR) ratios.

5. Our analysis shows that a radio-optical or radio–near-IR color selection technique could provide a potential means for detecting ULIG-type objects to $z \sim 1.6$.

Despite the lack of spectroscopic information, our study of a homogeneous population of faint radio sources has stressed the importance of dust on studies of intrinsic galaxy properties and their evolution at optical wavelengths. A future goal would be to obtain spectra or multicolor optical–near-IR photometry to better explore these sources and the validity of the simple stellar synthesis models presented in this paper. The ever improving resolution (and sensitivity) capabilities of optical–near-IR detectors over those feasible at (the longest) radio wavelengths requires robust identification techniques to better ascertain their properties. Likelihood ratios provide one such technique. The present study complements other deep optical studies of faint radio sources to constitute a statistically significant sample for inferring their nature and importance to galaxy evolution.

F. J. M. thanks Glenn Morrison and JoAnn O'Linger for valuable assistance with the data reduction and Rosalie Ewald for assistance with radio-optical image overlays. We thank the staff at Palomar Observatory for technical assistance during the observing run. This publication makes use of data products from the Two Micron All Sky Survey, which is a joint project of the University of Massachusetts and the Infrared Processing and Analysis Center/California Institute of Technology, funded by the National Aeronautics and Space Administration and the National Science Foundation. The National Radio Astronomy Observatory is operated by Associated Universities, Inc., under cooperative agreement with the National Science Foundation. This research has made use of the NASA/IPAC Extragalactic Database (NED), which is operated by the Jet Propulsion Laboratory, Caltech, under contract with the national aeronautics and space administration. F. J. M. acknowledges support from a JPL/NASA postdoctoral fellowship grant.

[9] Assumes $q_0 = 0.5$, $H_0 = 50$ km s^{-1} Mpc^{-1}.

REFERENCES

Benn, C. R., Rowan-Robinson, M., McMahon, R. G., Broadhurst, T. J., & Lawrence, A. 1993, MNRAS, 263, 98
Blain, A. W., Smail, I., Ivison, R. J., & Kneib, I.-P. 1999, MNRAS, 302, 632
Bruzual A., G., & Charlot, S. 1993, ApJ, 405, 538
Bryant, P. 1996, Ph.D. thesis, Caltech
Calzetti, D., Armus, L., Bohlin, R. C., Kinney, A. L., Koornneef, J., & Storchi-Bergmann, T. 2000, ApJ, 533, 682
Calzetti, D., Kinney, A. L., & Storchi-Bergmann, T. 1994, ApJ, 429, 582
———. 1996, ApJ, 458, 132
Ciliegi, P., et al. 1999, MNRAS, 302, 222
Condon, J. J. 1989, ApJ, 338, 13
———. 1992, ARA&A, 30, 575
———. 1997, PASP, 109, 166
Condon, J. J., Cotton, W. D., Greison, E. W., Yin, Q. F., Perley, R. A., Taylor, G. B., & Broderick, J. J. 1998, AJ, 115, 1693
Condon, J. J., & Yin, Q. F. 1990, ApJ, 357, 97
Cram, L. E. 1998, ApJ, 506, L85
Cram, L. E., Hopkins, A. M., Mobasher, B., & Rowan-Robinson, M. 1998, ApJ, 507, 155
Danese, L., De Zotti, G., Franceschini, A., & Toffolatti, L. 1987, ApJ, 318, L15
de Ruiter, H. R., Willis, A. G., & Arp, H. C. 1977, A&AS, 28, 211
Devriendt, J. E., Guiderdoni, B., & Sadat, R. 1999, A&A, 350, 381
Downes, A. J. B., Peacock, J. A., Savage, A., & Carrie, D. R. 1986, MNRAS, 218, 31
Fanaroff, B. L., & Riley, J. M. 1974, MNRAS, 167, 31P
Gavazzi, G., & Scodeggio, M. 1996, A&A, 312, L29
Genzel, R., et al. 1998, ApJ, 498, 579
Georgakakis, A., Mobasher, B., Cram, L., Hopkins, A., & Lidman, C. 1999, MNRAS, 306, 708
Goudfrooij, P., & de Jong, T. 1995, A&A, 298, 784
Gruppioni, C., Mignoli, M., & Zamorani, G. 1999, MNRAS, 304, 199
Haarsma, D. B., Partridge, R. B., Waddington, I., & Windhorst, R. A. 1999, 19th Texas Symposium on Relativistic Astrophysics and Cosmology, ed. J. Paul, T. Montmerle, & E. Aubourg (Gif-sur-Yvette: CEA Saclay), 600
Haarsma, D. B., Partridge, R. B., Windhorst, R. A., & Richards, E. A. 2000, ApJ, 544, 641
Hammer, F., Crampton, D., Lilly, S. J., Le Fèvre, O., & Kenet, T. 1995, MNRAS, 276, 1085
Helou, G., Soifer, B. T., & Rowan-Robinson, M. 1985, ApJ, 298, L7
Hopkins, A. M., Mobasher, B., Cram, L., & Rowan-Robinson, M. 1998, MNRAS, 296, 839
Kells, W., Dressler, A., Sivaramakrishnan, A., Carr, D., Koch, E., Epps, H., Hilyard, D., & Pardeilhan, G. 1998, PASP, 110, 1487
Kron, R. G., Koo, D. C., & Windhorst, R. A. 1985, A&A, 146, 38
Lonsdale, C. J., et al. 1998, in IAU Colloq. 179, New Horizons from Multi-Wavelength Sky Surveys, ed. B. McLean, D. Golombek, J. Hayes, & H. Payne (Dordrecht: Kluwer), 450
Lutz, D., Spoon, H. W. W., Rigopoulou, D., Moorwood, A. F. M., & Genzel, R. 1998, ApJ, 505, L103
Madau, P., Ferguson, H. C., Dickinson, M. E., Giavalisco, M., Steidel, C. C., & Fruchter A. 1996, MNRAS, 283, 1388
Madau, P., Pozetti, L., & Dickinson, M. 1998, ApJ, 498, 106
Maddox, S. J., Sutherland, W. J., Efstathiou, G., & Loveday, J. 1990, MNRAS, 243, 692
Metcalfe, N., Shanks, T., Fong, R., & Jones, L. R. 1991, MNRAS, 249, 498
Meurer, G., Heckman, T. M., Lehnert, M. D., Leitherer, C., & Lowenthal, J. 1997, AJ, 114, 54
Mitchell, K. J., & Condon, J. J. 1985, AJ, 90, 1957
Nakata, F., et al. 1999, MNRAS, 309, L25
Norris, R. P., Allen, D. A., & Roche, P. F. 1988, MNRAS, 234, 773
Okumura, S. K., Kawabe, R., Ishiguro, M., Kasuga, T., Morita, K. I., & Ishizuki, S. 1991, in Dynamics of Galaxies and Their Molecular Cloud Distributions, ed. F. Combes & F. Casoli (Dordrecht: Reidel), 425
Oort, M. J. A. 1987, A&AS, 71, 221
Pei, Y. C. 1992, ApJ, 395, 130
Prestage, R. M., & Peacock, J. A. 1983, MNRAS, 204, 355
Richards, E. A., Fomalont, E. B., Kellermann, K. I., Windhorst, R. A., Partridge, R. B., Cowie, L. L., & Barger, A. J. 1999, ApJ, 526, L73
Richards, E. A. 2000, ApJ, 533, 611
Rowan-Robinson, M., Benn, C. R., Lawrence, A., McMahon, R. G., & Broadhurst, T. J. 1993, MNRAS, 263, 123
Sanders, D. B., & Mirabel, I. F. 1996, ARA&A, 34, 749
Sanders, D. B., Soifer, B. T., Elias, J. H., Madore, B. F., Matthews, K., Neugebauer, G., & Scoville, N. Z. 1988, ApJ, 325, 74
Schaerer, D. 1999, in Building the Galaxies: From the Primordial Universe to the Present, XIXth Moriond Astrophysics Meeting, ed. F. Hammer et al. (Gif-sur-Yvette: Editions Frontières), in press (astro-ph/9906014)
Smith, H. E., Lonsdale, C. J., Lonsdale, C. J., & Diamond, P. J. 1998, ApJ, 493, L17
Soifer, B. T., Sanders, D. B., Madore, B. F., Neugebauer, G., Danielson, G. E., Elias, J. H., Lonsdale, C. J., & Rice, W. L. 1987, ApJ, 320, 238
Stetson, P. B. 1987, PASP, 99, 191
Sutherland, W., & Saunders, W. 1992, MNRAS, 259, 413
Thuan, X. T., & Condon, J. J. 1987, ApJ, 322, L9
Thuan, X. T., & Gunn, J. E. 1976, PASP, 88, 543
Thuan, X. T., Windhorst, R. A., Puschell, J. J., Isaacman, B. R., & Owen, F. N. 1984, ApJ, 285, 515
Turner, T. J., George, I. M., Nandra, K., & Mushotzky, R. F. 1997, ApJS, 113, 23
Windhorst, R. A., Fomalont, E. B., Partridge, R. B., & Lowenthal, J. D. 1993, ApJ, 405, 498
Windhorst, R. A., Miley, K. G., Owen, F. N., Kron, R. G., & David, C. K. 1985, ApJ, 289, 494